Two-year intercomparison of three methods for measuring black carbon concentration at a high-altitude research station in Europe

Sarah Tinorua[1,2], Cyrielle Denjean[1], Pierre Nabat[1], Véronique Pont[3], Mathilde Arnaud[1], Thierry Bourrianne[1], Maria Dias Alves[3], and Eric Gardrat[3]

[1]CNRM, Université de Toulouse, Météo-France, CNRS, Toulouse, France
[2]Now at Laboratory of Atmospheric Chemistry, Paul Scherrer Institute, Villigen, Switzerland
[3]Laboratoire d'Aérologie, UPS Université Toulouse 3, CNRS (UMR 5560), Toulouse, France

Correspondence: Sarah Tinorua (sarah.tinorua@psi.ch), Cyrielle Denjean (cyrielle.denjean@meteo.fr)

Abstract. Black carbon (BC) is one of the most important climate forcer with severe health effects. Large uncertainties in radiative forcing estimation and health impact assessment arise from the fact that there is no standardised method to measure BC mass concentration. This study presents a two-year comparison of three state-of-the-art BC measurement techniques at the high-altitude research station Pic du Midi located in the French Pyrenees at an altitude of 2877 m above sea level. A recently upgraded aethalometer AE33, a thermal-optical analyzer Sunset and a single-particle soot photometer SP2 were deployed to measure simultaneously the mass concentration of equivalent black carbon (M_{eBC}), elemental carbon (M_{EC}) and refractory black carbon (M_{rBC}), respectively. Significant deviations in the response of the instruments were observed. All techniques responded to seasonal variations of the atmospheric changes in BC levels and exhibited good correlation during the whole study period. This indicates that the different instruments quantified the same particle type, despite the fact that they are based on different physical principles. However the slopes and correlation coefficients varied between instrument pairs. The largest biases were observed for the AE33 with M_{eBC} values that were around 2 times greater than M_{rBC} and M_{EC} values. The principal reasons of such large discrepancy was explained by the too low MAC and C values recommended by the AE33 manufacturer and applied to the absorption coefficients measured by the AE33. In addition, the long-range transport of dust particles at PDM in spring caused significant increases in the bias between AE33 and SP2 by up to a factor 8. The Sunset M_{EC} measurements agreed within around 17% with the SP2 M_{rBC} values. The largest overestimations of M_{EC} were observed when the total carbon ~~concentration~~ concentrations were below 25 μgC cm^{-2}, which is probably linked to the incorrect determination of the OC-EC split point. Another cause of the discrepancy between instruments was found to be the limited detection range of the SP2, which did not allow the total detection of fine rBC particles. The procedure used to estimate the missing mass fraction of rBC not covered by the measurement range of the SP2 was found to be critical. We found that a time-dependent correction based on fitting the observed rBC size distribution with a multimodal lognormal distribution ~~are~~ is needed to accurately estimate M_{rBC} over a larger size range.

1 Introduction

Black carbon (BC), which results from incomplete combustion of fossil fuels, biofuel, and biomass, is one of the most impor-
tant short-lived climate forcer (IPCC, 2022). Due to its strong absorption in the visible wavelengths, it can reduce the amount
25 of sunlight reaching the surface, heat the atmospheric layer in which it resides and affects cloud formation, dissipation, precip-
itation with ensuing effects on atmosphere circulation through semi-direct radiative effects (Wang et al., 2016; Matsui et al.,
2018; Tang et al., 2020). When deposited on the cryosphere (e.g. glaciers, snow cover, and sea ice), BC can reduce the surface
albedo, thereby accelerating its melt (Réveillet et al., 2022; Jacobi et al., 2015). Moreover, BC poses a threat to human health
as it is considered as a carcinogen and a source of respiratory disease due to its nanometer size (Janssen et al., 2012).

30 BC mass concentration (M_{BC}) data are required to develop, assess, and improve emission inventories, climate and chemical-
transport ~~model simulations~~models, and mitigation strategies designed to both ~~reducing~~ reduce air pollution and climate
change. One major issue in M_{BC} measurements is related to the lack of internationally accepted standardised method to
measure it. Bond et al. (2013) discussed limitations in inferring its atmospheric concentration and highlighted inconsistencies
between different terminology and related measurement techniques. Petzold et al. (2013) defined a specific nomenclature for
35 BC according to its quantification method. Following the recommendation of the authors M_{BC} can be categorised into three
broad measurement techniques: (1) filter-based optical methods, which measure light attenuation and convert it to an equiva-
lent BC mass concentration (M_{eBC}); (2) ~~thermo-optical~~ thermal-optical analysis methods, which report elemental carbon mass
concentration (M_{EC}) as the mass concentration of carbon which is thermally refractory up to about 800 K (depending on
the analysis protocol); and (3) laser-induced incandescence (LII) methods, which measure refractory BC mass concentration
40 (M_{rBC}) as the incandescence signal of sampled particles after rapid heating to $\sim$4000K. Since there is not yet a universally
accepted M_{BC} quantification technique, it is extremely important to understand how the measurements vary between different
instruments and techniques and what are the reasons behind these potential differences~~are~~.

Filter-based optical methods are commonly used for M_{eBC} measurements at long-term research sites such as the Global Atmo-
sphere Watch (GAW), and the Aerosol, Clouds and Trace Gases Research Infrastructure (ACTRIS) programs because they are
45 inexpensive and easy to maintain. ~~Comparison~~ Previous comparisons of the different optical methods revealed discrepancies
up to 45% among instruments of the same type (Arnott et al., 2006; Chow et al., 2009; Müller et al., 2011; Laing et al., 2020;
Wu et al., 2015; Mason et al., 2018; Davies et al., 2018; Cuesta-Mosquera et al., 2021) and up to a factor of 5 when comparing
thermal-optical and LII methods (Healy et al., 2017; Laing et al., 2020; Slowik et al., 2007; Chirico et al., 2010; Sharma et al.,
2017). Quantifying M_{eBC} acquired by optical methods is challenging because it requires the assumption of a BC mass absorp-
50 tion cross section (MAC) value translating the absorption coefficient (σ_{abs}). Field and laboratory measurements have indicated
that MAC vary both temporally and spatially with values ranging from 3.8 to 58 m^2 g^{-1}(Wei et al., 2020). The wide range of
reported values is not surprising given that the MAC relies on the BC core diameter, coating thickness, chemical composition
and shape, which are expected to be influenced by a variety of spatio-temporal factors such as source type, transport pathway
and regional atmospheric composition and meteorology. Still further complications arise from the fact that the filter-based
55 optical methods are prone to several filter artifacts, including dependence of light attenuation on the filter tape loading, the

interference of aerosol light scattering with the absorption measurement and the multiple light scattering effects of the filter itself (Bond et al., 1999; Weingartner et al., 2003; Collaud Coen et al., 2010; Lack et al., 2014; Liousse et al., 1993; Schmid et al., 2006).

Thermal–optical and LII techniques are the most direct methods to measure M_{BC}. Both techniques make use of the high refrac-
toriness of BC to quantify its mass concentrations, although in different manners. There is considerable variability in results of field campaigns comparing M_{EC} and M_{rBC}. Some studies have shown that M_{rBC} measured by a SP2 and M_{EC} measured by a Sunset analyzer were consistent within measurement uncertainties (Laborde et al., 2012a; Corbin and Gysel-Beer, 2019; Miyakawa et al., 2016). Other studies have shown they can systematically differ by factors of up to 2.5 (Pileci et al., 2021; Zhang et al., 2016; Sharma et al., 2017). While the authors could not clearly assign the reasons for the ~~discrepancies to one~~
~~or the other method~~differences between the two methods, they found that various interferences from co-emitted species in the Sunset analyzer and the different particle size range covered by the two methods could be the reason for the discrepancies.

Most instrument inter-comparisons took place in the planetary boundary layer (PBL), whereas very few intercomparisons at upper altitudes are available in literature. Laing et al. (2020) found that M_{eBC} measured by an aethalometer at a US mountain site in the summer was 2 times higher than M_{rBC} measured by a SP2 when using the aethalometer manufacter's recommen-
dations for corrections. Observations in the free troposphere (FT) are more difficult to perform than at lower altitudes due to the lack of availability of suitable sites and due to adverse meteorological conditions. Airborne studies can overcome such problems but are usually limited to short time scales, and thus do not provide statistically representative information at seasonal time ~~scale~~scales. Moreover, distinguishing between signals, noise and inter-instrument uncertainty may become challenging at high altitude, as M_{BC} can be several orders of magnitude lower in the FT than in the PBL (Sun et al., 2021). These aspects have historically kept intercomparison of BC measurements in the FT very sparse.

In this work, we conducted a systematic comparison of three current state-of-the-art BC-monitoring instruments at the high-altitude research site of Pic du Midi in the French Pyrenees (PDM, 2877 m asl.). More specifically, the recently upgraded aethalometer (AE33, Magee Scientific, Berkeley, CA), analyses of filter samplings with a thermal-optical analyzer (Sunset) and an online single-particle soot photometer (SP2) were deployed continuously during two years to measure M_{eBC}, M_{EC}
and M_{rBC}, respectively. The purpose of this study is to evaluate the agreement between the three measurement techniques, to highlight the possible source of biases and to provide some recommendations on the use and data analysis of these different instruments.

2 Methods

2.1 Measurements site

The Pic du Midi research station (PDM, 42.93642°N, 0.14260°E) located in the South-West of France, is part of the Pyrenees mountain chain, with an altitude of 2877 m asl. This site belongs to the European Aerosols, Clouds, and Trace gases Research InfraStructure (ACTRIS-Fr) and to the Global Atmosphere Watch (GAW) program of the World Meteorological Organisation. It is often under the FT influence with limited local pollution around the site ~~(Collaud Coen et al., 2018; Gheusi et al., 2016; Tinorua et al., 2~~

Parameter	Instrument	Abbr.	Time Res.	Averag. Time	Measurement principle	Measurement uncertainty	Other notes
Refractory black carbon (rBC)	Single Particle Soot Photometer	SP2	1 sec	hourly	Laser induced incandescence of single particle	24.5% (quadratic sum of sampling flow, anisokinetic sampling errors and mass calibration factor errors (Schwarz et al., 2006))	Observed rBC mass distribution fitted by a daily multimodal lognormal size distribution
Equivalent black carbon (eBC)	7-wavelength Aethalometer with Dual Spot^{TM} technology	AE-33	2 min	hourly	Light absorption	35% (Zanatta et al., 2016)	Applying filter type correction using C = 1.39 (filter M8060), MAC = 7.77 m^2g^{-1}
Elemental carbon (EC)	Semi-continuous carbon aerosol analysis	Sunset	7 days	weekly	Light absorption and volatility	16% (Liu et al., 2013)	Analysing using EUSAAR-2 temperature protocol

Table 1. Summary of BC instruments and data analysis protocol used in this study

(Collaud Coen et al., 2018; Gheusi et al., 2016; Tinorua et al., 2024). It is therefore considered as a background mountain site. Air masses arriving at the PDM have various geographical origins coming from the Continental Europe, as well as over the Atlantic-Ocean, Iberian Peninsula and North Africa. Therefore, the PDM is a suitable site to study BC long-range transport in the lower FT.

2.2 Instrumentation

From February 2019 to January 2021, an important set of instruments has been deployed to measure BC microphysical, chemical and optical properties in the framework of the h-BC project (Tinorua et al., 2023)(Tinorua et al., 2024). Among them, three instruments were dedicated to the quantification of M_{BC}: a recently upgraded aethalometer (model AE33, Magee Scientific Company, Berkeley, CA, USA), a thermal-optical analyzer (Sunset Laboratory Inc., Tigard, OR, USA). and a single-particle soot photometer (SP2, DMT, Longmont, CO, USA). Table 1 summarises the main instrument characteristics and the uncertainty estimates for reported M_{BC}. Ambient BC-containing particles were sampled by a Whole Air Inlet, suitable for long-term observations, and placed 2 m above the building rooftop of PDM measurement station. The air passing through the inlet was heated at $\sim 20°C$ to prevent the relative humidity from exceeding 20% (Nessler et al., 2003).

2.2.1 The Single Particle Soot Photometer (SP2)

The SP2 measures M_{rBC} based on its incandescence capacity when heated to high temperatures. Its operating principle has been described previously (Baumgardner et al., 2012; Laborde et al., 2012b; Moteki and Kondo, 2010; Schwarz et al., 2006). To sum up, particles entering the instruments are passing through an Nd:YAG laser cavity, where they are heated up to 4000 K by the laser beam. If these particles contains rBC, they can then reach their incandescence point and produce a signal detected by two Avalanche Photodiodes. Since species internally mixed with BC particles will evaporate before the rBC incandescence, the

measured mass only takes into account the amount of rBC mass without interference from its potential coating. The intensity of this signal is proportional to the rBC mass. The incandescence peak height is converted to an individual rBC mass using a
110 calibration factor and then a rBC density of 1800 kg m^{-3} (Bond and Bergstrom, 2006) is used to convert the rBC mass into ~~an~~ a rBC mass equivalent diameter.

The calibration was performed using monodispersed fullerene soot (Alfa Aesar, lot #FS12S011) selected by a differential mobility analyzer and applying a second order polynomial fit.

The SP2 data were processed using the PySP2 code, a computer code written in Python that derives the rBC mass concentration
115 and mixing state from SP2 measurements ~~(Tinorua et al., 2023)~~(Tinorua et al., 2024). The rBC mass was quantified from $\sim$ 0.68 to 320 fg, corresponding to $90 < D_{\text{rBC}} < 700$ nm. This size range was set by comparing the particle number concentration of the size-selected fullerene soot particles measured by the SP2 against the one measured by a Condensation Particle Counter (CPC, model 3772, TSI Inc., Shoreview, USA). Typical rBC size distributions tend to fall a consistent larger range from a few nanometers to a few micrometers (Bond et al., 2013). To date, there have been three approaches to estimate and correct for the
120 rBC mass undetected by the SP2. All these methods are based on fitting the measured rBC size distribution with lognormal distribution and ~~extrapolating the measured rBC size distribution to larger and smaller sizes to estimate the "missing" rBC~~ estimating the ambient fraction of rBC mass outside the SP2 measurement range, hereafter referred as $R_{\text{fit/meas}}$ and calculated using Eq. 1:

$$R_{\text{fit/meas}} = \frac{M_{\text{rBC,fit}} - M_{\text{rBC,meas}}}{M_{\text{rBC,meas}}} \tag{1}$$

125 where $M_{\text{rBC,fit}}$ is the fitted rBC size distribution ~~and~~ between 1 and 1000 nm and $M_{\text{rBC,meas}}$ the measured rBC size distribution ~~by the~~ in the detection size range of the SP2.

(i) The most widely used approach is to fit the campaign average size distribution with a single and monomodal lognormal distribution and to derive a single correction factor of the mass concentration, hereafter called $R_{\text{fit/meas}}$ (Schwarz et al., 2006; Laborde et al., 2012a; Metcalf et al., 2012; Zanatta et al., 2018; Liu et al., 2010; Ko et al., 2020). (ii) Another method consists
130 in fitting the campaign average size distribution with a multimodal lognormal distribution using the sum of two to four modes (Cappa et al., 2019; Raatikainen et al., 2017; Zhao et al., 2019). (iii) A last procedure proposed in the present study consists in calculating a time-dependent correction factor by fitting with a sum of several lognormal modes the rBC size distribution averaged on a shorter time period than the campaign duration. This approach is supported by the fact that rBC size distribution can vary as a function of the sources and aging processes (Cappa et al., 2019; Takahama et al., 2014). In this study, all three
135 methods were applied in order to assess the sensitivity to the correction approach. Bounds of the fitting parameters d_{g} and σ_{g} were fixed as following : Mode 1 : $50 < d_{\text{g}} < 100$ nm and $1.2 < \sigma_{\text{g}} < 3$; Mode 2 : $150 < d_{\text{g}} < 250$ nm and $1.3 < \sigma_{\text{g}} < 2.9$; Mode 3 : $350 < d_{\text{g}} < 500$ nm and $1 < \sigma_{\text{g}} < 3$ with d_{g} and σ_{g} the geometric mean diameter and the geometric standard deviation, respectively. The resulting uncertainty on M_{rBC} is estimated to be around 24.5 %, ~~taking into account measurement uncertainties on the M_{rBC} correction (see section 3.1) and the relative precision of SP2-derived M_{rBC} (unit-to-unit variability as determined~~

140 ~~by Laborde et al. (2012a))~~ corresponding to the quadratic sum of the 20 % uncertainty on the mass calibration factor, the 10 % uncertainty for anisiokinetic sampling errors and the 10 % uncertainties on the flow calibration (Schwarz et al., 2006).

2.2.2 The ~~thermo-optical analyzer~~ thermal-optical analyser Sunset

Weekly integrated filter-sampled particles were analyzed using an EC/OC analyser (Sunset Laboratory Inc., Tigard, OR, USA), hereafter referred to as Sunset. We used the EUSAAR–2 heating protocol with transmittance correction (Cavalli et al., 2010).
145 This protocol was specifically developed for aerosol typically encountered at European background sites and it was recently selected as the European standard thermal protocol to be applied in air quality networks for the measurements of total carbon (TC), organic aerosol (OC) and EC in particulate matter samples (European Committee for Standardisation Ambient air, 2017; EN16909:2017).

The measurement principle is based on the different volatilisation temperatures of OC and EC (Bauer et al., 2009). Briefly,
150 aerosols were collected on a pre-burnt quartz fiber filter at PDM and thermally desorbed in the Sunset ~~Analyzer~~ analyser following a temperature gradient. A first step allowed the OC desorption by progressively heating to 500-700°C in an inert atmosphere ~~with~~ made of pure helium (He). A second step brought the filter at higher temperature ($\sim$ 850 °C) in an oxidizing atmosphere composed of 98% helium and 2% dioxygen to induce the EC desorption. At each temperature step the OC (in the inert atmosphere) and the EC (in the oxydised atmosphere) are oxydised to carbon dioxide and then catalitycally reduced to
155 methane, which is quantified by a nondispersive infrared (NDIR) detector, and associated to a mass of OC or M_{EC}.

Due to temperature elevation, some OC can be pyrolised and thus be desorbed during the second step of the procedure, leading to an overestimation of the sampled M_{EC}. This artefact due to the so-called Pyrolytic Carbon (PyrC) is corrected using thermal-optical transmittance correction. The split-point, determined in order to separate EC and refractory OC, is defined as the time at which the transmission through the filter in the second step (oxidised atmosphere) during the EC and ~~PC~~ PyrC desorption
160 equals the transmission through the filter in the first step (inert atmosphere) before ~~PC~~ PyrC formation (i.e. initial value of transmission). The distinction between PyrC and native EC is based on two assumptions : (1) During the oxidative phase, PyrC is the first to completely evolve before native EC and (2) PyrC and native EC have the same mass absorption cross section (MAC) (Yang and Yu, 2002). Thus, the total OC mass on the filter is the sum of the four OC fractions (OC1, OC2, OC3 and OC4) and the total EC mass on the filter is the sum of the four EC fractions (EC1, EC2, EC3 and EC4) minus the PyrC mass
165 determined optically (which is converted in OC fraction).

The Sunset calibration was performed using a sucrose ($C_6H_{12}O_6$) solution containing two different known TC surface loading (35.16 and 42.527 μgC cm^{-2}), spiked on blank filters. Several blank filters were analysed over the campaign and the resulting transmission intensity was introduced as an offset in the data. The limit of detection (LOD) of M_{EC} is generally estimated using different methods based on filter blank measurements. The first one consists in averaging M_{EC} across several blank
170 filter samples (Sciare et al., 2011). Bauer et al. (2009) estimated the LOD by calculating the 95th percentile off the standard deviation over zero air measurements. The method recommended by EN16909:2017 consists in calculating the average Sunset blank filter value from a high number of blank measurements and add two times its standard deviation (Jaffrezo et al., 2005; Karanasiou et al., 2020). The last method that was used here consists in taking three times the standard deviation of several

blank measurements as proposed by Brown et al. (2019). By using 22 blank measurements, blank levels of 0.17 and 0.70 μgC cm^{-2} were obtained for EC and TC, respectively (using an average sampling volume of 440 m^3). The LOD on EC is similar to the one of 0.18 μgC. cm^{-2} obtained by Zheng et al. (2014), who studied the variations of the LOD among different protocols, and close to the LOD of 0.1 μgC cm^{-2} determined by Bauer et al. (2009).

2.2.3 The dual-spot aethalometer AE33

A dual-spot aethalometer (model AE33, Magee Scientific, USA) was used to quantify M_{eBC}. This instrument measures the attenuation of light at seven wavelengths (370, 470, 520, 590, 660, 880 and 950 nm) through a filter where particles are continuously collected. M_{eBC} was calculated from the attenuation coefficient σ_{ATN} measured at 880 nm because other light-absorbing particles, such as brown carbon (BrC) and mineral dust, absorb significantly less at this wavelength (Samset et al., 2018). In the aethalometer, the change in attenuation with time is caused by both the increasing mass of eBC deposited on the filter (i.e. loading effect), and the scattering by particles and filter matrix (Weingartner et al., 2003; Segura et al., 2014). To overcome the loading effect, a compensation algorithm has been incorporated into the AE33 using an on-line dual-spot technology (Drinovec et al., 2015).

Following Drinovec et al. (2015) σ_{ATN} and M_{eBC} can be derived by applying Eq. 2 and Eq. 3, respectively:

$$\sigma_{ATN} = \frac{S.\frac{\Delta ATN}{100}}{F(1-\zeta).(1-k\Delta ATN).\Delta T} \tag{2}$$

$$M_{eBC} = \frac{S.\frac{\Delta ATN}{100}}{F(1-\zeta).C.(1-k\Delta ATN).\Delta T.MAC} \tag{3}$$

where S is the filter surface area loaded with the sample, ΔATN the variation of attenuation on this surface on the spot, F the measured flow rate passing through the instrument corrected by the leakage factor ζ (here equals to 0.01), C the multiple scattering coefficient, k the loading factor parameter and Δt the sampling duration of aerosols in the aethalometer fixed at 20 minutes.

M_{eBC} was first determined using the default instrumental filter constant C of 1.39 for the M8060 filter tape and a MAC of 7.77 m^2 g^{-1} at 880 nm. In Section 3.5, we have estimated the hourly and weekly C×MAC values that allow to better match the M_{eBC} with M_{rBC} and M_{EC} at PDM.

To limit biases caused by extreme values, M_{eBC} under the lower detection limit of the AE33 (0.005 μg m^{-3}) and over the 95th percentile of the distribution were filtered before the analysis.

2.3 Other parameters

Aerosol scattering coefficients (σ_{sca}) were retrieved by an integrating nephelometer (model Aurora 3000, Ecotech Pty Ltd, Knoxfield, Australia) at 450, 525 and 635 nm and the Scattering Angström Exponent (SAE) was then calculated between 450

and 635 nm ($SAE_{450-635}$). Absorption coefficients were derived from the attenuation measurements of the AE33 at 470 and 660 nm, and then converted to 450 and 635 nm using the Absorption Ångström Exponent calculated between 370 and 470 nm ($AAE_{370-470}$) and between 590 and 660 nm ($AAE_{590-660}$), respectively.

A scanning mobility particle sizer (SMPS), which consists in a differential mobility analyzer (DMA; model 3071, TSI Inc., Shoreview, MN, USA) and a condensation particle counter (CPC; model 3772, TSI Inc., Shoreview, MN, USA), has been used to measure the aerosol size distribution between 12.6 and 532.6 nm.

To avoid biases linked to inlet artifacts and local pollution, periods where when precipitation events, high humidity (95%) and high CO concentrations (>200 ppb) occurred were removed from the dataset. The Hysplit model (Hybrid Single-Particle Lagrangian Integra has been used to retrieve the precipitation events along the 72-h trajectory of air masses arriving at the measurement site. The model was initialised to the PDM altitude, using 3-hourly atmospheric data of 1×1 ° spatial resolution from the Global Data Assimilation System (GDAS) of the National Centers for Environmental Prediction (NCEP). Weekly averages were calculated from hourly SP2 and AE33 data when at least 70% of the hourly data were available. All data were converted to standard temperature and pressure (STP) using local meteorological data.

3 Results

3.1 Sensitivity of rBC mass concentration to size distribution processing from the SP2 measurements

Figure 1 presents the campaign-average mass weighted rBC size distribution derived from the SP2. Two distinct peaks can be seen at D_{rBC}= 130 nm and D_{rBC}= 180 nm. A third coarse coarser mode seems to raise around 490 400 nm. From this figure, it can clearly be seen that the SP2 does not measure the rBC size distribution over its full size range. We evaluated three different approaches described in Section 2.2.1 to correct M_{rBC} for the rBC mass undetected by the SP2. The extend to which the different approaches contributes to uncertainty on the overall M_{rBC} was quantified by comparing the fitted to observed M_{rBC} on the SP2 detection size range ($90 < D_{rBC} < 700$ nm). When using a 1-mode representation, the fitting procedure gave a mode centered on D_g = 153 nm on average over the 2-year campaign while the three modes of the trimodal fit peaks at $D_{g,1}$ = 98 nm, $D_{g,2}$ = 177 nm and $D_{g,3}$ =377 nm. A first direct comparison between the fitting procedure shows that both approaches represent well the measurements for D_{rBC} between 90 and 150 nm. However,the 1-mode fit overestimates M_{rBC} for D_{rBC} between 150 and 230 nm and completely misses the largest mode above around 400 nm, while both are well represented by the trimodal approach. As a first conclusion, the trimodal curve generally better follows the measurements, and in particular for rBC diameter above 150 nm.

Figure 2 shows the ratio between M_{rBC} estimated from the fitting approaches and fitted between 1 and 1000 nm and the one derived from the observation ($M_{rBC,fit}/M_{rBC,meas}$) over the D_{rBC} range covered by the SP2 for the different fitting approaches throughout the campaign (Figure 2a) and the overall statistical results (Figure 2b). Considering all data points from the campaign, the unimodal fit tends to slighly underestimate M_{rBC} by around 1.6% regardless of the selected averaging time. When using a trimodal lognormal function, the overall statistics for these two quantities agree more closely within 0.4 %. However, both the variability and the systematic bias in the $M_{rBC,fit}/M_{rBC,meas}$ ratio are considerably smaller when fitting the rBC size
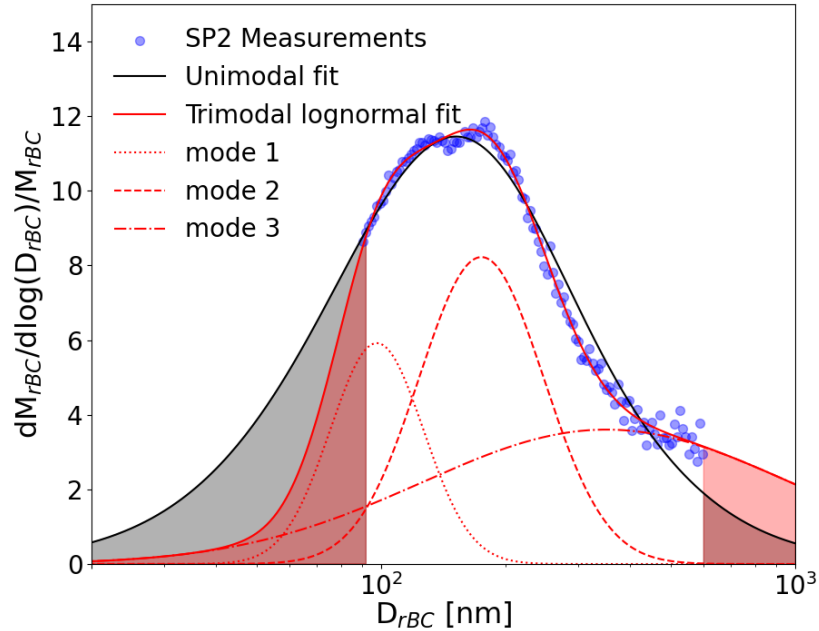
Figure 1. rBC core size distribution averaged over the campaign and fitted with a unique (in black lines) or a sum of three log-normal functions (in red line). The three modes are in red dotted lines. Blue dots represent the SP2 measurements over its size detection range. The black and red shaded areas represent the rBC mass fraction missed by the SP2 and recalculated when applying a unimodal or a trimodal fitting procedure, respectively. Data were normalised by the sum of M_{rBC} and averaged over the campaign.

235 distribution with a trimodal lognormal distribution and on a daily basis. The evolution of the $M_{rBC,fit}/M_{rBC,meas}$ ratio over the 2-year measurement period shown in Fig. 2a illustrates that $M_{rBC,fit}$ differs regularly from $M_{rBC,meas}$ by more than 5% for every fitting procedure, and even more ~~on~~ in autumn and winter. In fact, as shown in Figure S1 in the ~~Supplements~~Supplement, the averaged rBC size distribution observed in autumn and winter are more noisy than the one in summer and spring. In particular, the second mode usually peaking at around ~~170-180~~180 nm is less clearly defined in autumn and winter with some

240 outliers above the general distribution. The third coarse mode at $D_{rBC} \sim$ ~~500~~400 nm exhibits also a higher variability in cold seasons compared to the ones fitted in spring and summer. ~~Tinorua et al. (2023)~~Tinorua et al. (2024) showed that winter was characterised by lower M_{rBC} with some rBC-containing particles injected from the boundary layer during the day, compared to summer when an additional long-range transport of rBC-containing particles occurred. Thus, the noisier rBC size distributions in winter and autumn could be due to the low daily M_{rBC} which leads to greater uncertainties in the fitting procedure,

245 and/or more sporadic variability in M_{rBC} due to the PBL dynamics in winter. Overall these results suggests that neglecting the day-to-day variability of rBC size distribution at PDM may lead to an overestimation of M_{rBC}.

~~Although the overall bias between $M_{rBC,meas}$ and $M_{rBC,fit}$ remained low (< 2% on average over the 2-year campaign) regardless the approach chosen, larger differences in rBC size distribution can be observed for D_{rBC} < 90 nm (Fig. 2a).~~ The extrapolation of rBC size distribution towards lower and larger sizes lead to a missed mass fraction $R_{fit/meas}$ calculated

250   using Eq. 1 of around 25% and 15% for the unimodal and multimodal fit, respectively. Therefore, in the following, all reported M_{rBC} are corrected with the multimodal fit on a daily basis. ~~It~~ Although the overall bias between $M_{rBC,meas}$ and $M_{rBC,fit}$ remained low (< 2% on average over the 2-year campaign) regardless the approach chosen, it can be seen in Figure 1 that the largest differences between the 1-mode and the 3-modes fitting approaches occurs for D_{rBC} < 90 nm. It is important to note that the lack of measurements below 90 nm complicates the estimation of the missing mass fraction. Since it is possible

255   that discrepancies between instruments arise from the extrapolation of rBC size distribution towards lower and larger sizes, the influence of the estimated fraction of undetected rBC particles on the biases between instruments will be investigated in Section 3.4.
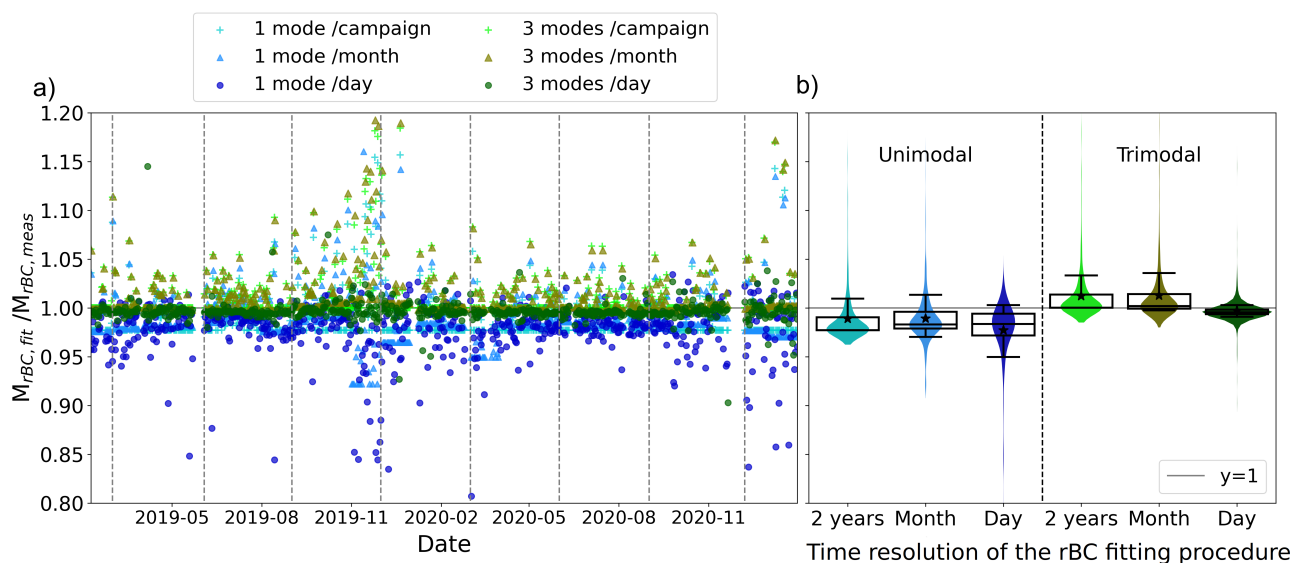
Figure 2. a) Time series and b) statistics of $M_{rBC,fit}/M_{rBC,meas}$ calculated between ~~90~~ 1 and ~~700~~ 1000 nm when representing the rBC size distribution with one (lightblue ~~and~~ to darkblue) or three (light green ~~and green~~ to darkgreen) modes and when fitting on the mean campaign (crosses), monthly (triangles) or daily (plain circles) size distribution. Violin plot represent the probability density function of $M_{rBC,fit}/M_{rBC,meas}$. Boxes and whiskers represent the 25th, 75th, 10th and 90th percentiles. Lines and stars ~~shows medians~~ show median and mean values.

3.2 Overview of rBC, EC and eBC mass concentrations measured by the SP2, Sunset and AE33 and their relationship

Figure 3 shows the temporal variation and frequency distribution of M_{rBC}, M_{EC} and M_{eBC}, which are respectively BC mass concentrations measured by the SP2, Sunset and AE33 from January 2019 to February 2021. Table S1 in the ~~Supplements~~ Supplement reports statistical analysis of M_{rBC}, M_{EC} and M_{eBC}. Over the whole period the mean values ($\pm$ GSD) of M_{EC}, M_{rBC}, and M_{eBC} were 54.7 ($\pm$ 25.3), 36.4 ($\pm$ 28.4), and ~~75.5~~ 78.5 ($\pm$ 54.3) ng m^{-3}, respectively. All techniques respond to seasonal variations of the atmospheric changes in BC levels. Average concentrations were around 2-4 times (depending on the measurement technique) higher in summertime than in wintertime, with monthly averages ranging from a minimum of 14.2-44.8 ng m^{-3} in December to a maximum of 65.6-142.3 ng m^{-3} in July. This seasonal variation is similar to those reported at the high-altitude European sites of Jungfraujoch in Switzerland for M_{eBC} measurements (Bukowiecki et al., 2021) and Montseny in Spain for M_{EC} measurements (Zanatta et al., 2016). At ~~the~~ PDM, this seasonality was attributed to the combined effects of less precipitation and a larger contribution of long-range transport from biomass burning sources during summer ~~(Tinorua et al., 2023)~~(Tinorua et al., 2024).

Figure 4 shows scatterplots of time-resolved relationship between M_{rBC}, M_{EC} and M_{eBC} over the campaign using distinct colors for each month. Positive correlations were observed between all instruments with Pearson's r values ranging from 0.66 to 0.80. All linear regressions were based on an assumption of a zero intercept.

Considering all data points, the largest bias is observed between the AE33 and the SP2 measurements (fig. 4c.), with M_{eBC} higher by a factor 1.96 than M_{rBC} on average. The good Pearson's r value of 0.80 shows that the bias is systematic. The correlation slope is almost parallel with the 1:1 line, meaning that there is an offset error of M_{eBC} compared to M_{rBC}. Considering the colors of the points, there is no link between the time of the year and the value of the bias.

The SP2 and Sunset measurements appear to have the best agreement with a correlation slope of 1.17 between M_{EC} and M_{rBC}. As shown in Figure 4a, the correlation between the Sunset and the SP2 measurements degrades for M_{EC} lower than 50 ng m^{-3}. The threshold M_{EC} value can also be observed to a lesser extent on the relationship between the AE33 and Sunset measurements with a slight break in the correlation slope below 50 ng m^{-3} (Figure 4b). These results point to a loss of Sunset sensitivity below this limit value. The reasons behind these results will be investigated in the next section.
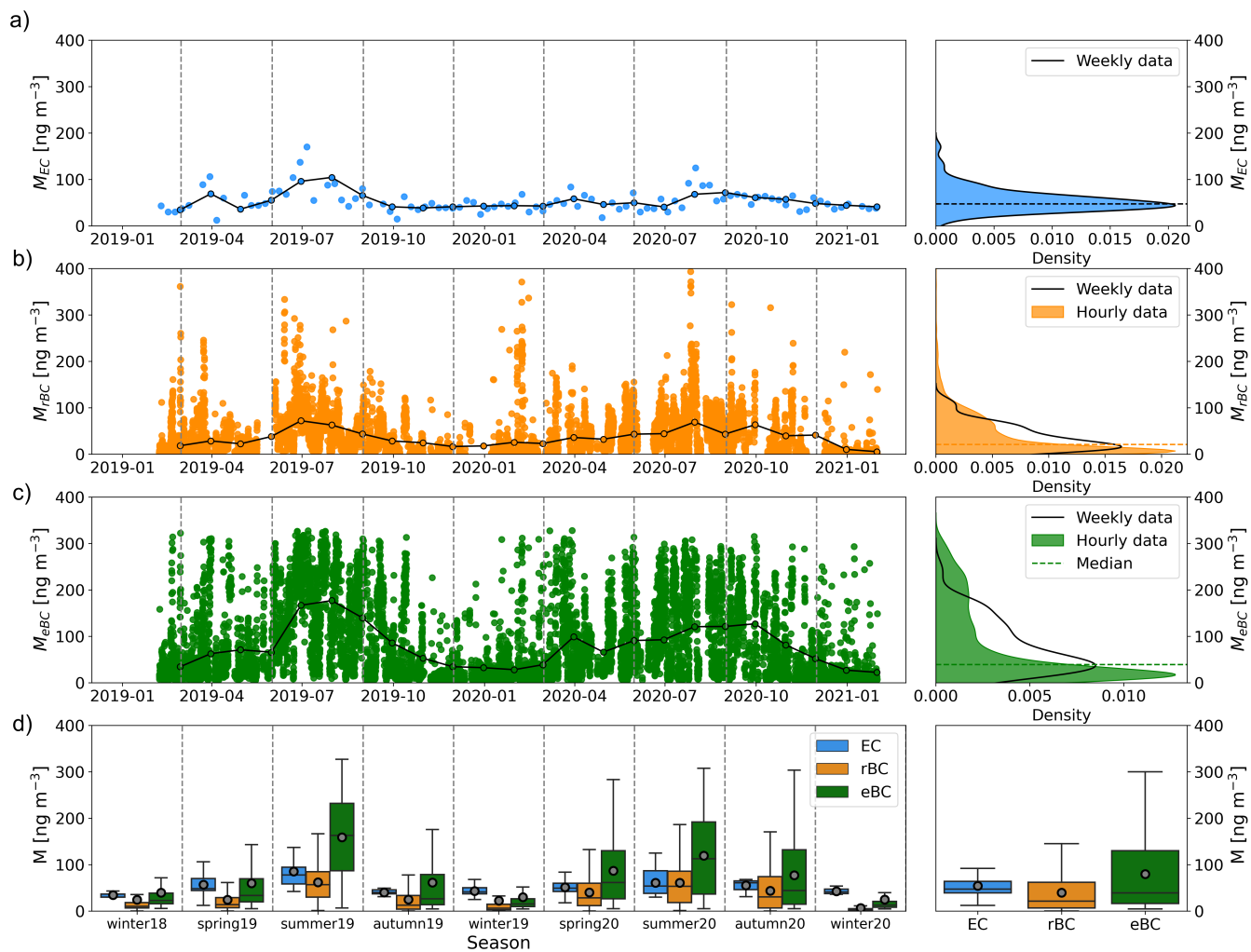
Figure 3. Time series (left) and statistical analysis (right) of (a) M_{EC}, (b) M_{rBC} and (c) M_{eBC} measured during the campaign. Dots connected with lines represent monthly averages and ~~little~~ isolated dots represent hourly data. For (b) and (c), Probability Distribution Functions of M_{rBC} and M_{eBC} was calculated over hourly data in colors and over resampled data on the time resolution of the Sunset in black lines. (d) Seasonal boxplot of M_{EC}, M_{rBC} and M_{eBC}.
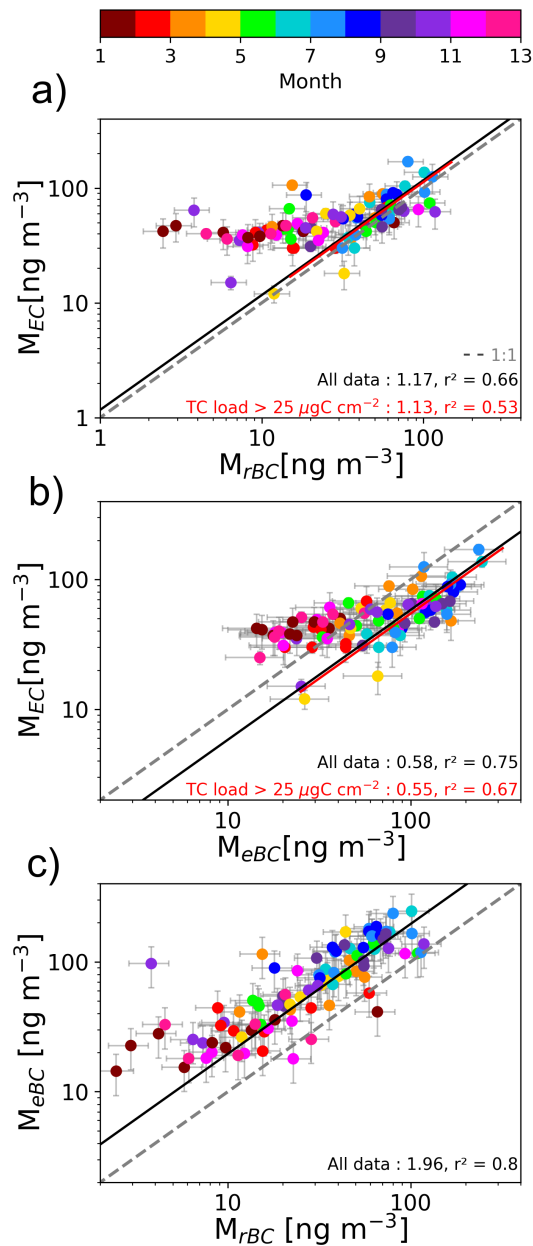
Figure 4. Scatterplot of the relationship between (a) M_{EC} versus M_{rBC}, (b) M_{EC} versus M_{eBC} and (c) M_{eBC} versus M_{rBC} over to the ~~two~~ whole measurement period. The correlation coefficients are shown for each plot. *For M_{EC} vs. M_{rBC} and M_{EC} vs. M_{eBC}, the slope excluding data where the TC load was lower than 25 μgC cm^{-2} has also been calculated.

3.3 Biases on EC mass concentration measured by the Sunset : filter underloading and charring effect

The main challenges in isolating EC from TC analysis are the possible artifacts during OC/EC separation. In a study from the EMEP Co-operative Programm for Monitoring and ~~Evaluation of~~ Evaluationof the Long-range Transmission of Air Pollutants in Europe implying 36 instruments measuring M_{EC} over Europe (EMEP/CCC – Report 1/2018, ~~),~~ https://projects.nilu.no/ccc/reports/cccr1_ Data_Report_2016_FINAL.pdf), a bias is mentioned in the determination of the OC/EC split point at low TC concentrations, which usually ~~led~~ lead to an overestimation of M_{EC}. However there is no detail provided to explain the effects.

Figure 5a shows how the filter TC loading ~~influence~~ influences the biases between M_{EC} and M_{rBC}. The same analysis has not been carried out for M_{EC} to M_{eBC} ratio because of the multiple sources of biases in M_{eBC} (i.e. section 3.5). A systematic positive bias and a wide dispersion of the M_{EC}/M_{rBC} ratio can be observed at TC contents below 25 μgC cm^{-2} (Mean $\pm$ GSD of 3.08 $\pm$ 2.71). Above this TC value, no significant dependence on the filter loading can be distinguished with a lower mean ($\pm$ GSD) M_{EC}/M_{rBC} ratio of 2.35 $\pm$ 3.29. A large fraction of samples (42%) with TC loading below 25 μgC cm^{-2} was measured in winter. When data with a TC load below 25μgC cm^{-2} are eliminated, the bias between M_{rBC} and M_{EC} is reduced, with a decrease in the value of the slope from 1.17 to 1.13 (see Fig. 4a). By contrast, excluding data with a TC load below 25μgC cm^{-2} leads to a slope of M_{EC} vs. $M_{\text{~~rBC~~ eBC}}$ farthest from unity (0.55 against 0.58 considering all data, see Fig. 4b). This is for sure due to the compensating effect of data with a TC load lower than 25μgC cm^{-2} on the overestimation of M_{eBC} compared to M_{EC}, thus leading to a slope slightly closer to 1.

Our results are consistent with the sharp reduction in the repeatability and reproducibility at low TC loadings (below 10 μgC cm^{-2}) reported during an inter-laboratory comparison for the measurement of M_{EC} performed within the European project ACTRIS-2 on ambient aerosol samples collected at a regional background site in Italy (EMEP/CCC–Report 1/2018). Conversely, Pileci et al. (2021) did not find any increased random noise or systematic bias caused by low TC surface loading. However, Fig S2 in the Supplement shows that the superimposition of our data with theirs indicate a similar trend with a wide dispersion of M_{EC}/M_{rBC} ratio below 25 μgC cm^{-2}. As explained in Zheng et al. (2014), the threshold TC load for accurate ~~thermo-optical~~ thermal-optical analysis can vary with location and season due to the variation of thermal properties among carbonaceous particles collected on the filter.

We further investigate the potential causes of the Sunset bias with a special focus on the charring correction used to derive M_{EC} with the EUSAAR-2 protocol. Optical correction is an essential component of the ~~thermo-optical~~ thermal-optical method to remove measurement artifacts in OC and EC caused by charring of some OC components. Without correction, the charred fraction of OC, also called PyrC, would be reported as part of EC, leading to an ~~overestimate~~ overestimation of M_{EC}. Charring depends on many factors, including the amount and type of organic compounds, temperature steps in the analysis, the residence time at each temperature step, and the presence of certain inorganic constituents or BrC (Yu et al., 2002; Subramanian et al., 2007; McMeeking et al., 2009).

Figure 5b presents the M_{EC}/M_{rBC} ratio as a function of the M_{EC}/M_{TC} ratio to investigate if biases arise from the split between OC and EC. No dependence of M_{EC}/M_{rBC} to M_{EC}/M_{TC} ratio can be observed. This result differs from that obtained by Pileci et al. (2021) for five different field campaigns performed with different instruments. This could suggest that the quantification
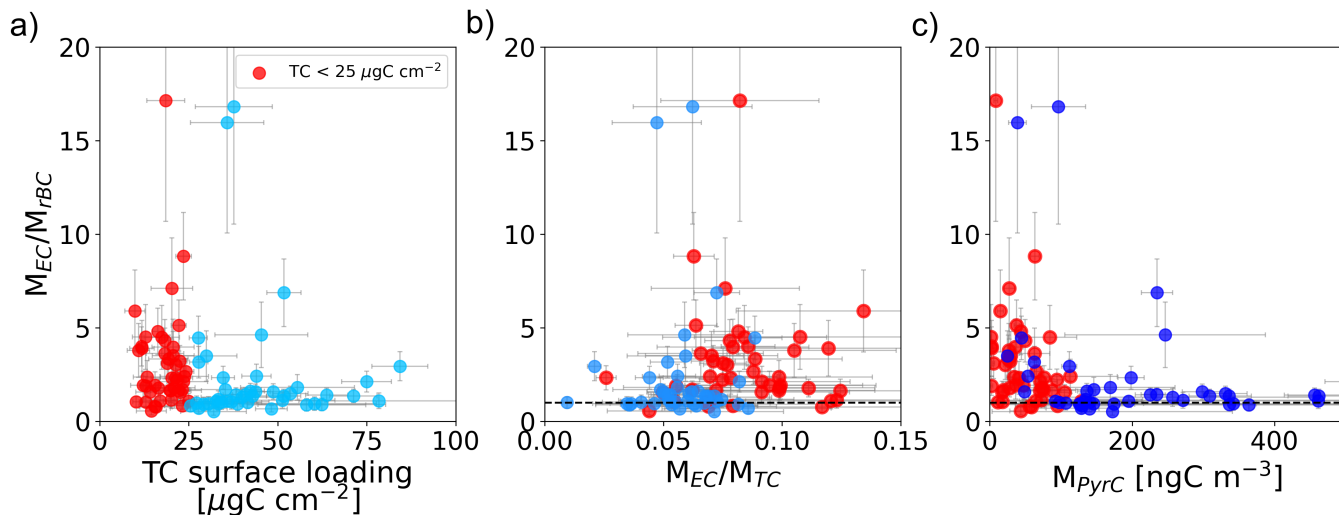
Figure 5. M_{EC}/M_{rBC} as a function of a) Total Carbon surface loading, b) M_{EC}/M_{TC} and c) M_{PyrC}. Points have a weekly time resolution. Red ~~circles~~ dots highlights data where the TC loading is under $25\mu g\ cm^{-2}$

of M_{EC}/M_{TC} ratio is more controlled by the instrument characteristic and set-up than the instrument-specific analysis-by-analysis variability.

Two ~~distinct~~ different patterns can be distinguished for M_{EC}/M_{rBC} as a function of M_{PyrC} in Figure 5c. A wide dispersion of
320   M_{EC}/M_{rBC} ratio for M_{PyrC} below $140\ ngC\ cm^{-3}$ can be observed with a mean ($\pm$ GSD) of 3.17 ($\pm$ 3.40), whereas M_{EC}/M_{rBC} are closer to 1 (1.63 $\pm$ 1.29) above this threshold value. All the data with M_{PyrC} above $140\ ngC\ cm^{-3}$ exhibited a TC loading over 25 $\mu gC\ cm^{-2}$. By contrast below M_{PyrC} of $140\ ngC\ m^{-3}$ most samples (73%) exhibit a TC loading lower than 25 μgC cm^{-2}. Interestingly the remaining samples with M_{PyrC} below $140\ ngC\ cm^{-3}$ and TC loading above 25 $\mu gC\ cm^{-2}$ show a mean M_{EC}/M_{rBC} value of around 3.40. This result indicates a possible underestimation of M_{PyrC} for these samples that could
325   explain some of the bias between M_{EC} and M_{rBC}.

Another possible measurement artifact can arise from the presence of dust and BrC particles as mentioned previously by Liu et al. (2022) and Karanasiou et al. (2020). However, as will be explained in section 3.5, the sporadic nature of dust events at PDM compared to the long sampling duration of the Sunset did not allow to identify samples with significant Saharan dust contribution. Furthermore, ~~Tinorua et al. (2023)~~ Tinorua et al. (2024) found a very low contribution of BrC to the aerosol
330   absorption at PDM. Ammerlaan et al. (2015) also highlighted a possible influence of the laser stability on M_{EC} bias. Here, a deep analysis of the blank filters did not reveal laser instabilities. In addition, the analysis of the baseline of the transmission signal in the thermograms did not allow us to identify potential causes of the overestimation of M_{EC}.

In the following, all Sunset data for which TC content is lower than 25 $\mu gC\ cm^{-2}$ have been eliminated ~~of~~ from the analysis.

3.4 Biases on rBC mass concentration measured by the SP2 due to the presence of undetected small/large rBC-containing particles

As shown in section 3.1 and Figure 1, the limited SP2 detection range ($90 < D_{rBC} < 700$ nm) can lead to an underestimation of M_{rBC}. In this section we investigate if the M_{EC}/M_{rBC} mass discrepancy could be partially explained by the presence of BC particles outside the SP2 detection size range. M_{rBC} has been corrected for the missing mass concentration outside the SP2 detection range using an extrapolation method based on daily multi-modal fits to the measurement (i.e. section 2.2.1 and 3.1). Figure 6 shows the campaign-averaged mass-weighted rBC size distribution classified into four ranges of fractional amount of missing mass fraction ($R_{fit/meas}$). $R_{fit/meas}$ increases strongly as the proportion of mode 1 (i.e. centered at around 100 nm) increases. This mode 1 becomes predominant when $R_{fit/meas}$ exceed 0.1 while the mode 2 (i.e. centered at around 180 nm) becomes secondary. Meanwhile, the proportion of the mode 3 (i.e. centered at around ~~500 nm) remain~~ 400 nm) remains rather constant for all ranges of $R_{fit/meas}$. As shown in Table 2, the extrapolated mass fraction under the lower detection range of the SP2 ($D_{rBC} < 90$ nm) increases from 7.9 to 19 % as $R_{fit/meas}$ increases from values ≤ 0.1 to values > 0.3. By contrast, above the higher detection range ($D_{rBC} > 700$ nm), the extrapolated mass fraction is very low with values around 2.5 % and is not correlated to $R_{fit/meas}$ values. Overall, these results show that the presence of small rBC particles below the lower detection limit of the SP2 is the main contributor to the extrapolation calculations, whereas the contribution of large rBC particles above the higher detection limit is rather negligible.

Given the remote location in the Pyrenees and apparent distance from fresh BC source regions of the PDM site, it is expected that rBC particles sampled at this site are aged with relatively large sizes. Regarding the large contribution of ultrafine rBC particules, their presence at PDM is surprising, but could be explained by two hypotheses. First, it is possible that some periods with local influences of rBC emission ~~may~~ still remain despite the filtering of ~~isolating~~ isolated spikes of CO (i.e. Section 2). However, the $R_{fit/meas}$ shows no correlation with M_{rBC} (see figure S3 in the ~~Supplements~~Supplement), meaning that the presence of ultrafine rBC does not preferentially occur during local pollution event when M_{rBC} were sporadically very high. In fact, an opposite trend can be observed with higher $R_{fit/meas}$ (> 0.2) under low M_{rBC} conditions (< 30 ng m^{-3}). Second, these ultrafine rBC-containing particles could be produced by aviation emissions. Modal diameters of nonvolatile particle size distributions in aircraft turbine exhaust range from 15 to 40 nm (Lobo et al., 2015; Durdina et al., 2017, 2019) while particles from unfiltered gasoline direct injection and diesel engines have larger count mean diameter values ranging from 50 to 100 nm (Burtscher, 2005; Momenimovahed and Olfert, 2015). Recently, BC mass emissions was estimated to be around 100-1000 g/km^2 per year above the Pyrenees region (Zhang et al., 2019b) if only taking into account the global civil aviation. ~~Tinorua et al. (2023)~~ Tinorua et al. (2024) showed that the dominant air mass origin at PDM is the North-Atlantic Ocean, where around 14% of the total BC mass emissions from civil aviation occurs (Zhang et al., 2019a). To further investigate the role of small particles on the M_{rBC} biais, the aerosol number size distributions grouped by M_{EC}/ M_{rBC} ratios has been plotted in Fig. 7. The size distribution for which the highest ratios between M_{EC} and M_{rBC} has been observed clearly shows a contribution of small particles (<20 nm) up to 2 times higher than when the bias on the M_{EC}/ M_{rBC} ratio was negative or neutral, supporting that the M_{rBC} underestimation compared to M_{EC} is probably due to undetected small rBC-containing particles.
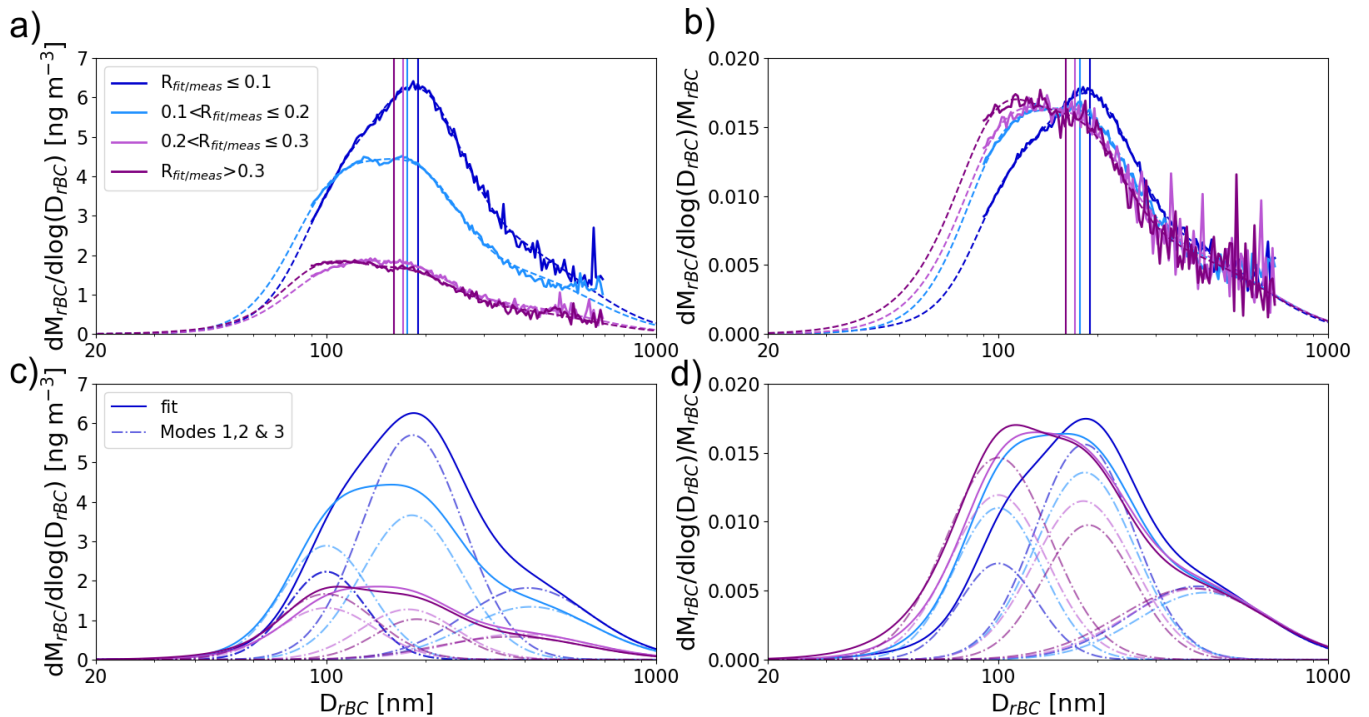
Figure 6. a) Mass size distribution of rBC core measured by the SP2 colored as a function of the missing mass correction factor $R_{fit/meas}$. Vertical lines show the geometric diameter of each rBC mass size distribution. ~~The fitting procedure is represented by dotted lines.~~ b) same as a) but normalised by the total rBC mass. c) Same as a) but showing the position of the three modes with the fitting procedure represented by dotted lines. d) Same as c) but normalised by the total rBC mass.

In order to estimate the extent to which the extrapolation in rBC size distribution contributes to uncertainty in the overall M_{rBC}, ~~Figure~~ Fig. 8 shows the mass-weighted rBC size distribution classified into different ranges of M_{EC}/M_{rBC} ratio : a

370 significant negative bias ($M_{EC}/M_{rBC} \leq 1 - \Delta(M_{EC}/M_{rBC})$, with $\Delta(M_{EC}/M_{rBC})$ representing the uncertainty in M_{EC}/M_{rBC}), an agreement within the uncertainty range ($1 - \Delta(M_{EC}/M_{rBC}) < M_{EC}/M_{rBC} \leq 1 + \Delta(M_{EC}/M_{rBC})$) and a significant positive bias ($M_{EC}/M_{rBC} > 1 + \Delta(M_{EC}/M_{rBC})$). An examination of the ~~shape of mass size distribution~~ shapes of rBC core mass size distributions of rBC core in ~~figure~~ Fig. 8 did not reveal any variability for the different ranges of M_{EC}/M_{rBC} values. From these results we can not conclude any influence of the SP2 ~~limiting~~ limited detection size range on the discrepancy between

375 the SP2 and Sunset. However, it is important to note that the modal diameters and widths for Mode 1 and 3 are particularly uncertain as these modes occur near the lower and higher detection limit of the SP2. Uncertainties in the position and width for these mode may contribute to uncertainty in the total M_{rBC}. In addition it is possible that (1) the extrapolation of the first mode peaking at ~ 100 nm is inaccurate for masses lower than 90 nm~~as a large part of this mode occurs below~~, which is the

$R_{fit/meas}$	Total fitted mass M_{rBC} [ng m^{-3}]	M_{rBC} for D_{rBC} <90 nm [ng m^{-3}]	Extrapolated %age to D_{rBC} <90 nm	M_{rBC} for D_{rBC} >700 nm [ng m^{-3}]	Extrapolated %age to D_{rBC} >700 nm
≤ 0.1 Mean (GSD)	3.74 (4.16)	0.295 (0.366)	7.90 (8.79)	$8.49 \cdot 10^{-5}$ ($9.75 \cdot 10^{-5}$)	2.27 (2.35)
]0.1 ;0.2] Mean (GSD)	3.00 (2.62)	0.385 (0.354)	12.8 (13.5)	$6.79 \cdot 10^{-5}$ ($6.56 \cdot 10^{-5}$)	2.26 (2.51)
]0.2 ;0.3] Mean (GSD)	1.29 (1.54)	0.195 (0.234)	15.2 (15.2)	$3.10 \cdot 10^{-5}$ ($4.27 \cdot 10^{-5}$)	2.41 (2.76)
>0.3 Mean (GSD)	1.28 (1.91)	0.247 (0.447)	19.4 (23.5)	$2.52 \cdot 10^{-5}$ ($3.57 \cdot 10^{-5}$)	1.97 (1.87)
All Mean (GSD)	2.46	0.290 (0.360)	11.8 (12.1)	$5.49 \cdot 10^{-5}$ ($6.97 \cdot 10^{-5}$)	2.23 (2.34)

Table 2. Extrapolated mass fraction of M_{rBC} outside the SP2 size detection range for each $R_{fit/meas}$.
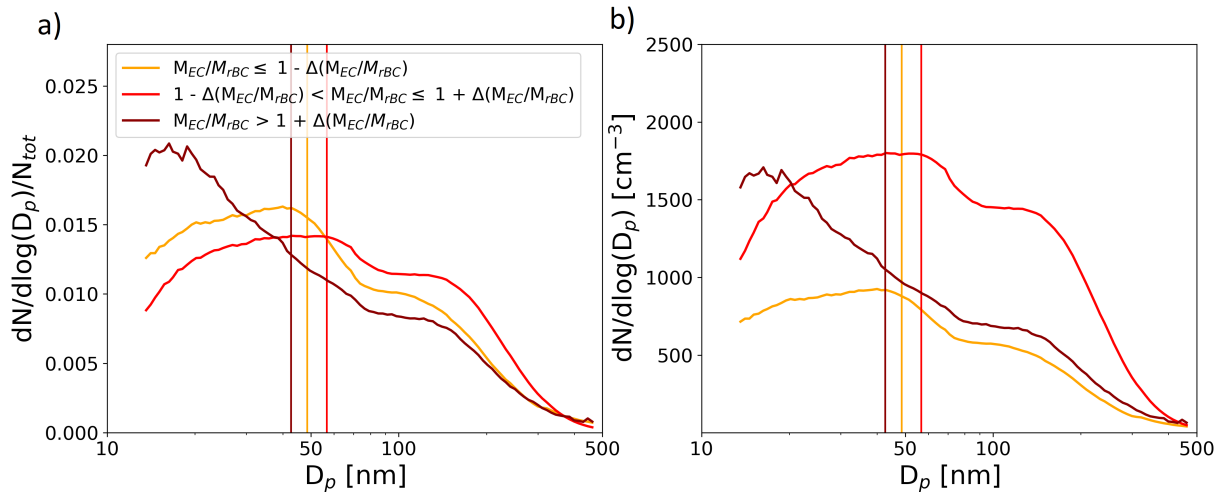
Figure 7. a) Number size distribution of aerosols measured by the SMPS , colored by M_{EC}/M_{rBC} ranges of values. b) is the same as a) but normalised by the total aerosol number concentration. Vertical lines highlight geometrical diameter corresponding to the color of the M_{EC}/M_{rBC} range.

lower size detection limit of the SP2 or (2) the SP2 missed the detection of a mode that is centered at lower diameter than the
380   lower limit of detection of the SP2.
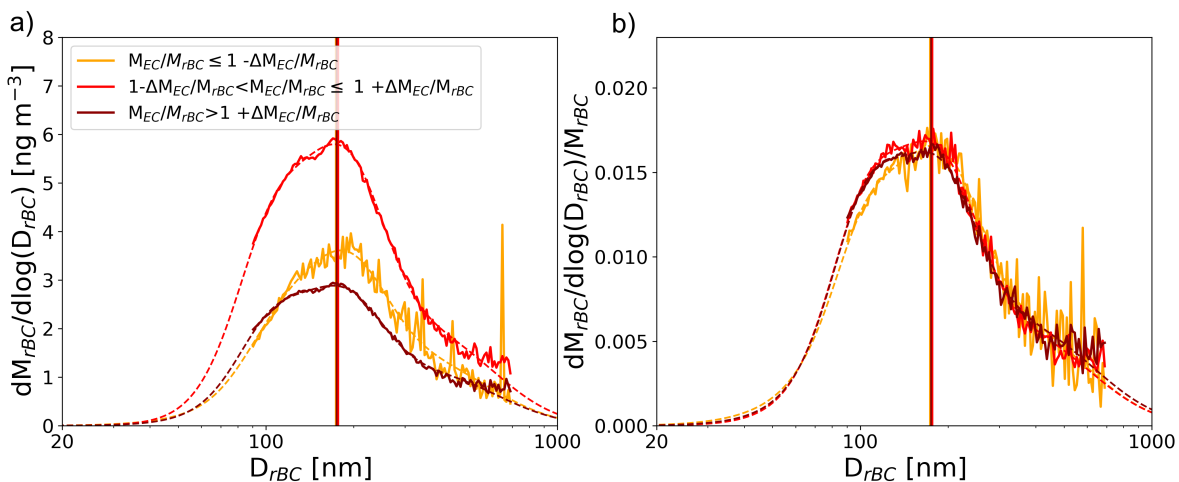
Figure 8. a) Mass size distribution of rBC core measured by the SP2, colored by M_{EC}/M_{rBC} ~~, grouped by~~ ranges of values. b) is the same as a) but normalised by the total rBC mass. Vertical lines ~~highlights~~ highlight geometrical diameter corresponding to the color of the M_{EC}/M_{rBC} range.

3.5 Biases on eBC mass concentration measured by the AE33

The main uncertainties in the M_{eBC} inferred from the AE33 measurement are the MAC used to calculate M_{eBC} from the absorption coefficient and the correction due to multiple scattering of particles sampled on the filter (Arnott et al., 2005; Bond et al., 1999; Collaud Coen et al., 2010; Weingartner et al., 2003). The multiple-scattering correction factor C depends on the

385 optical properties of the aerosol collected on the filter and the filter tape used. A constant MAC value of 7.77 m^2 g^{-1} is recommended by the AE33's manufacturer to convert $\sigma_{\mathrm{abs},880}$ to M_{eBC}, which is representative of optical properties of fresh BC particles (Bond et al., 2013). Nonetheless a wide range of MAC of BC from ~~5.9 to 54.8~~ 3.8 to 58 m^2 g^{-1} at 880 nm has been reported from field and laboratory measurements (Wei et al., 2020). This variability is due to the diversity of BC microphysical and chemical properties, which are related to their emission sources (Schwarz et al., 2008) and the effects of ageing processes

390 during the transport in the atmosphere (Ko et al., 2020; Sedlacek et al., 2022; Peng et al., 2016).

We first recalculated hourly (weekly) C×MAC values obtained at PDM by dividing σ_{ATN} at 880 nm by M_{rBC} (M_{EC}). Figure 9a shows that daily C×MAC values calculated with M_{rBC} are around 2 to 3 times higher than those recommended by the manufacturer, with a median value of 27.8 m^2 g^{-1}, against 10.8 m^2 g^{-1} for the constructor's value. In addition, a clear seasonal pattern can be observed with median values of 24.5 m^2 g^{-1} and 31.3 m^2 g^{-1} in spring and summer, respectively. C×MAC

395 values calculated using M_{rBC} from the SP2 are around 21 % higher than those obtained using M_{EC} from the Sunset (Figure 9c) with median values of 25.2 and 20.8 g^{-1}, respectively, despite averaging SP2 over the same time resolution as Sunset (Figure 9b). However, similar seasonal variability in the C×MAC values was obtained using M_{EC} and M_{rBC}, although no statistical
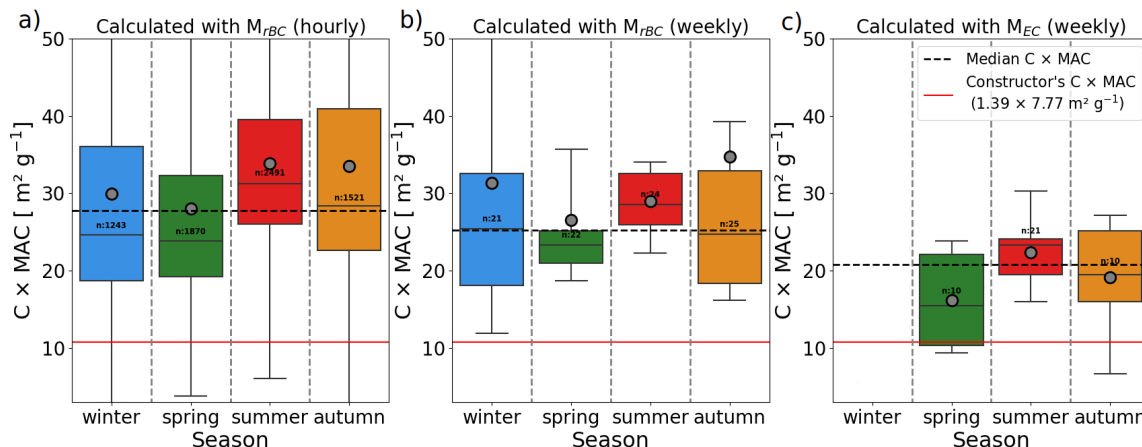
Figure 9. C×MAC as a function of the season calculated with a) M_{rBC} in an hourly basis, b) M_{rBC} averaged over the sampling period of the Sunset, and c) M_{EC}, excluding TC loading < 25 μgC cm^{-2}. Constructor's values are represented with a red solid line while median values are represented with a black dashed line. For b), the median is calculated excluding winter's value to be in agreement with c). Boxes, lines, black dots and whiskers indicate 25th percentile, 75th percentile, median, mean, 10th percentile and 90th percentile, respectively.

values could be obtained in winter due to too low M_{EC} values during this season. This is consistent with the seasonal trend of C values obtained at Montsec d'Ares in the Spanish Pyrenees by Yus-Díez et al. (2021) using σ_{abs} measured by a MAAP (Multi-Angle Absorption Photometer). In addition, Pandolfi et al. (2014) found also higher MAC values at 637 nm in summer than in spring at this site.

In order to investigate the cause of the seasonal variation of C×MAC, we plotted ~~on Figure~~ in Fig. 10 the correlation between C×MAC and $\Delta M_{rBC}/\Delta CO$ ratio for each season. The $\Delta M_{rBC}/\Delta CO$ ratio has been shown to be a good tracer of the rBC combustion source and wet deposition (Baumgardner et al., 2002; Taylor et al., 2014). Here ΔM_{rBC} and ΔCO were estimated using the approach presented in ~~Tinorua et al. (2023)~~Tinorua et al. (2024). Briefly, the hourly ΔCO were obtained by subtracting the hourly CO concentrations by the background CO concentrations estimated from the rolling 5th percentile of the values on a 14-day time window. ΔM_{rBC} was considered to be equal to M_{rBC}, thus assuming that the background M_{rBC} is zero. Air masses for which precipitation occurred along 72-h back trajectories performed with the Hysplit model were removed in order to investigate the influence of rBC sources only. Lower C and MAC values are generally observed in the literature for rBC-containing particles emitted from fossil combustion compared to those emitted from biomass combustion (Laing et al., 2020; Sedlacek et al., 2022; Healy et al., 2015; McMeeking et al., 2014; Denjean et al., 2020). A significant increase of C×MAC can be observed in Fig. 10 for $\Delta M_{rBC}/\Delta CO$ < 2 ng m^{-3} ppbv^{-1} in every season except for spring, suggesting that a BC source-dependant correction should be applied to the AE33.
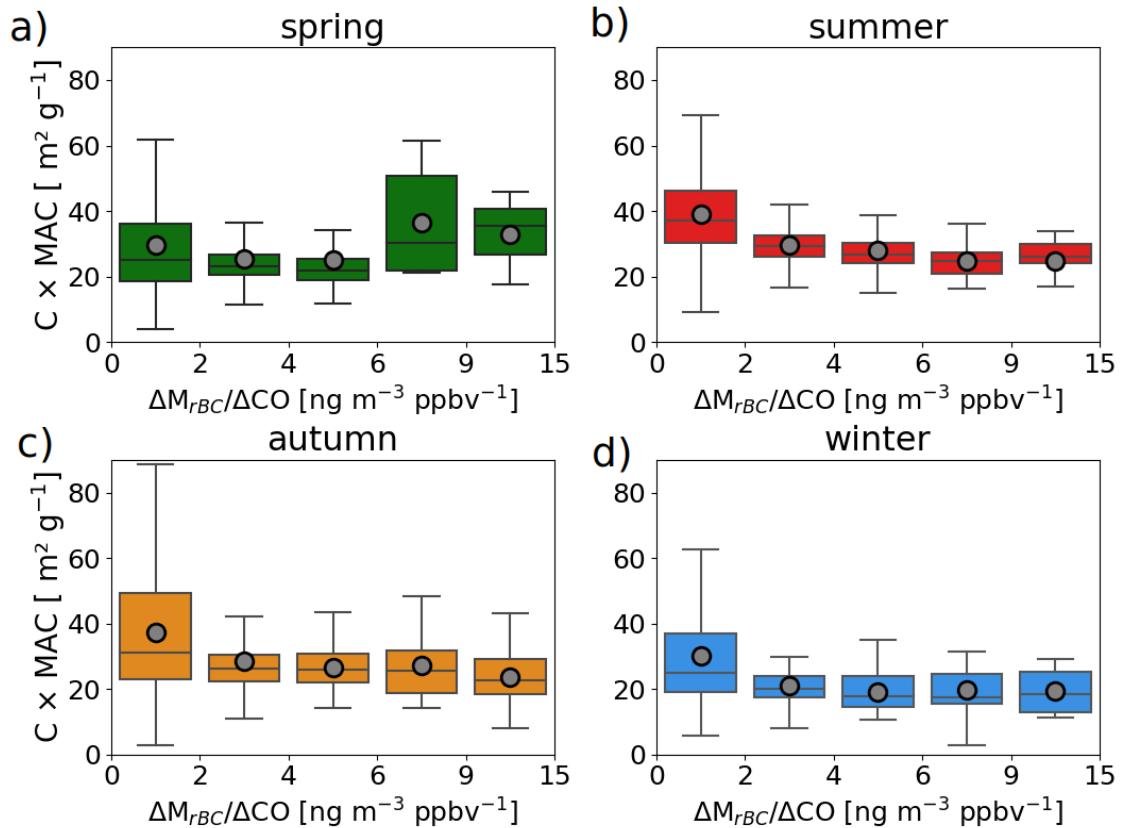
Figure 10. a) to d) C×MAC as a function of the $\Delta M_{\text{rBC}}/\Delta CO$ emission ratio for spring, summer, autumn and winter, respectively. Boxes, lines, black dots and whiskers indicate 25th percentile, 75th percentile, median, mean, 10th percentile and 90th percentile, respectively.

The ~~different trend observed~~ absence of correlation between C×MAC and $\Delta M_{\text{rBC}}/\Delta CO$ in spring may be due to a measurement artifact during this season~~,~~ , such as the dominant presence of dusts particles which can affect the C correction of the AE33 (cf. Fig. 10a and associated text). In order to study the influence of other co-existing light-absorbing particles on C×MAC, a classification of the dominant aerosol type sampled at the PDM was performed. This classification, detailed in ~~Tinorua et al. (2023)~~Tinorua et al. (2024), is based on the daily analysis of the spectral aerosol optical parameters AAE and SAE. Aerosols with AAE > 2 and SAE < 0.25 were classified as dust-dominated, aerosols with AAE > 2 and SAE > 1.5 were classified as BrC and AAE > 1.5 characterised aerosol mixtures containing dust particles and/or BrC (Kirchstetter et al., 2004; Lack and Cappa, 2010).

Figure 11~~b~~ a shows $M_{\text{eBC}}/M_{\text{rBC}}$ ratio as a function of the season and the dominant aerosol type. The same analysis could not be carried out for $M_{\text{eBC}}/M_{\text{EC}}$ ratio due to the short duration of the dust events reaching PDM (<1-2 days) compared to the duration of aerosol sampling for Sunset analyses (1 week). The level of agreement between M_{eBC} and M_{rBC} over the 2-year

425   campaign degrades by a factor of 2 when aerosols were dominated by dust particles (averaged M_{eBC}/M_{rBC} ± STD of 6.7 ± 3.6 and 3.2 ± 6.3 during and outside dust events, respectively). The bias is the greatest in spring with M_{eBC}/M_{rBC} ratio reaching 8.6 ± 3.7 (see Fig 11a). This seasonality is due to a stronger influence of dust events transported in the Pyrenees in spring ~~(Tinorua et al., 2023)~~(Tinorua et al., 2024). It should be noted that no BrC-dominated events were observed at PDM, probably due to their low lifetime in the atmosphere (around 1 day) (Forrister et al., 2015; Wong et al., 2019). In addition, no

430   increase of M_{eBC}/M_{rBC} ratio is observed for aerosols composed of a mixing of rBC with dust and/or BrC particles, suggesting that only the predominance of dust particles in the aerosol lead to significant biases in M_{eBC} retrieval. Previous studies showed that a higher C value should be applied for dust samples (Yus-Díez et al., 2021; Di Biagio et al., 2017). Using the same instrumentation as this study, Yus-Díez et al. (2021) showed that a C value of around 3.95 should be used for correcting multiple scattering artefacts in the AE33 during Saharan dust outbreaks. As shown in the equation (2), an increase of C value would

435   lead to decrease of M_{eBC} values and thus a decrease of M_{eBC}/M_{rBC} ratio from 6.7 to 2.3. Thus, a C readjustment taking into account the presence of dusts significantly improves the M_{eBC}/M_{rBC} ratio. Nonetheless, a bias is still present even without the presence of dusts, suggesting an inappropriate MAC value regarding eBC measured at PDM.
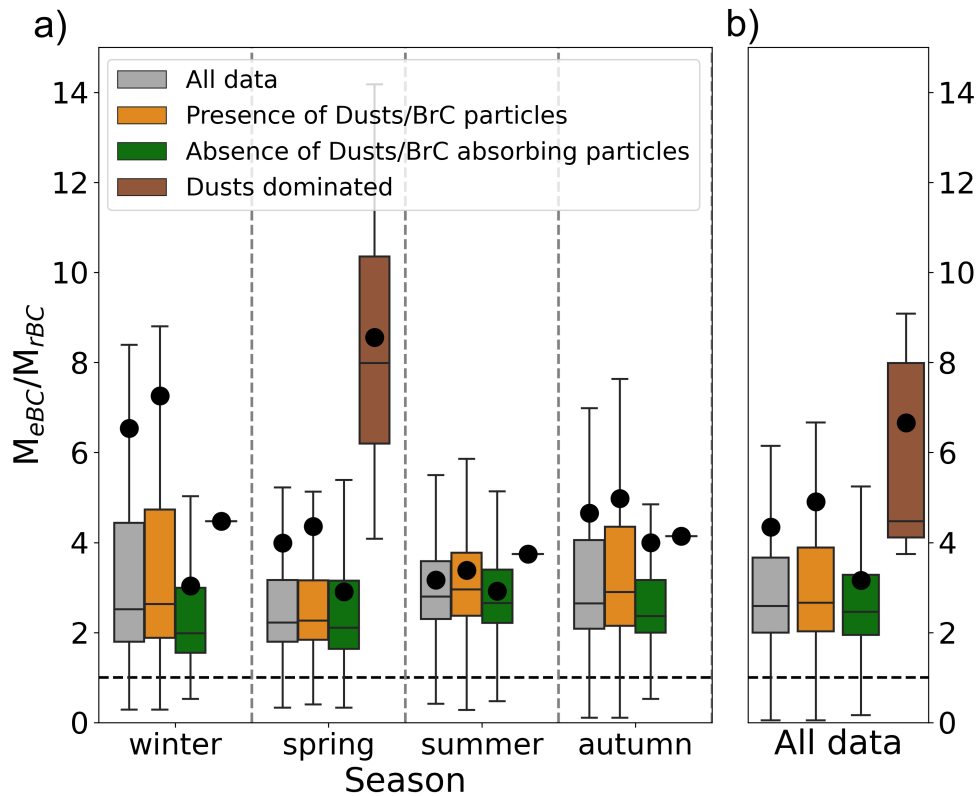
Figure 11. M_{eBC}/M_{rBC} as a function of the dominant aerosol type a) as a ~~unction~~ function of the season and b) over the 2-year measurement campaign. Boxes, lines, black dots and whiskers indicate 25th percentile, 75th percentile, median, mean, 10th percentile and 90th percentile, respectively.

4   Summary, conclusions and recommendations

Three of the most widely used instruments to measure BC mass concentration have been compared during a two-years measurement campaign at the high altitude site Pic du Midi in the french Pyrenees. The agreement between a SP2, ~~an~~ a AE33 and a Sunset measuring refractive BC (rBC), equivalent BC (eBC) and elemental carbon (EC), respectively, ~~have~~ has been studied and the causes of variability have been investigated.

All techniques responded to seasonal variations of the atmospheric changes in BC levels and exhibited good ~~correlation~~ correlations during the whole study period. This indicates that the different instruments quantified the same particle type, despite the fact that they are based on different physical principle. However the slopes varied between instrument pairs. The largest biases were observed for the AE33 M_{eBC} values that were larger by a factor of around 2 than SP2 M_{rBC} and Sunset M_{EC} values. The SP2 and Sunset measurements appear to have the best agreement with an average bias by around 17 % between M_{EC} and M_{rBC}.

450 However large overestimation of M_{EC} compared to M_{rBC} and M_{eBC} is observed when M_{TC} was lower than 25 μgC cm^{-2} of TC surface loading on the filter. Our analyses indicate a possible underestimation of M_{PyrC} for some of these samples that could partly explain the positive bias in Sunset measurements. This threshold TC value is higher than the value of 10 μgC cm^{-2} obtained during the multiple-Sunset intercomparison study performed at a PBL background site in Italy (EMEP/CCC–Report 1/2018). We ~~note~~ can notice that the aerosol types measured in this last intercomparison study may be very different to those

455 studied here, and therefore this result could indicate a dependence of the lower quantification limit of the Sunset to the thermal properties of the sampled carbonaceous particles. This threshold is a real issue for remote sites where low aerosol concentrations prevail and it raises the need for alternative measurement techniques at low TC loading.

The main source of bias in M_{rBC} measurements is found to be the limited size detection range of the SP2, which ~~do~~ does not allow the detection of all rBC particles. Sensitivity tests based on different fitting approaches varying in terms of time resolu-

460 tion and number of lognormal modes ~~has~~ have been carried out. While most studies use a fit with a single mode and averaged over the entire campaign, this approach does not adequately reproduce the rBC size distribution observed at PDM. Our results indicate that ~~considering~~ a considerion of the daily variation and multimodal shape of rBC size distribution is required in the fitting procedure for accurately quantify M_{rBC} at PDM.

The systematic positive bias in AE33 compared to SP2 and Sunset was attributed to the C×MAC values applied for the M_{eBC}

465 retrievals. The best agreement between M_{eBC} and both M_{rBC} and M_{EC} was obtained when C×MAC values were around 1.9 to 2.3 times higher than those recommended by the manufacturer. C×MAC values were found to be seasonal-depend and strongly linked to the source of rBC (determined using $\Delta M_{rBC}/\Delta$CO tracer). Another cause of bias in AE33 ~~is~~ measurements was found to be the sampling of dust particles that causes a large overestimation of M_{eBC} by up to a factor of 8. The incorrect C value applied during dust events may be the main cause of such a discrepancy.

470 Based on the results and specific issues presented above, this study points out some recommendations for improving the assessment of M_{EC}, M_{rBC} and M_{eBC} :

1. The low detection sensitivity in separating accurately OC and EC at low TC contents with the Sunset ~~Analyser~~ analyser makes the use of this instrument tricky at some remote and background measurement sites under low pollution conditions.

475 2. A special attention should be paid to the rBC procedure used to estimate the missing mass fraction of rBC not covered by the SP2 ~~measurement~~ detection size range. The temporal resolution and the number of modes required to fit the rBC size distribution can vary greatly from one region to another and from one season to another.

3. We recommend to remove periods under strong dust events from the AE33 dataset, which could lead to a large overestimation M_{eBC}.

480 4. If possible, the systematic deployment of an additional on-line instrument to measure absorption coefficient unaffected by filter artefacts would be very useful to constrain the correction factor C applied in AE33 retrievals.

Data availability. rBC, EC and eBC data are available upon request to the authors.

Competing interests. The authors declare that they have no conflict of interest.

Acknowledgements. This work received funding from the French national program LEFE/INSU and Météo-France. Observation data were
485 collected at the Pyrenean Platform for Observation of the Atmosphere P2OA (http://p2oa.aero.obs-mip.fr) in the frame of the SNO-CLAP
(National Observatory Service for CLouds and Aerosols Properties). P2OA facilities and staff are funded and supported by the University
Paul Sabatier Toulouse 3, France, and CNRS (Centre National de la Recherche Scientifique). We especially thank the staff of the Pic du
Midi platform (Observatoire Midi-Pyrénées) for their technical assistance. We acknowledge the SNO ICOS-France and ACTRIS-France for
supporting aerosol observations at PDM, data collection, processing and dissemination.

References

Ammerlaan, B. A. J., Jedynska, A. D., Henzing, J. S., and Holzinger, R.: On a possible bias in elemental carbon measurements with the Sunset thermal/optical carbon analyser caused by unstable laser signal, Atmospheric Environment, 122, 571–576, https://doi.org/10.1016/j.atmosenv.2015.09.076, 2015.

Arnott, W. P., Hamasha, K., Moosmüller, H., Sheridan, P. J., and Ogren, J. A.: Towards Aerosol Light-Absorption Measurements with a 7-Wavelength Aethalometer: Evaluation with a Photoacoustic Instrument and 3-Wavelength Nephelometer, Aerosol Science and Technology, 39, 17–29, https://doi.org/10.1080/027868290901972, publisher: Taylor & Francis _eprint: https://doi.org/10.1080/027868290901972, 2005.

Arnott, W. P., Walker, J. W., Moosmüller, H., Elleman, R. A., Jonsson, H. H., Buzorius, G., Conant, W. C., Flagan, R. C., and Seinfeld, J. H.: Photoacoustic insight for aerosol light absorption aloft from meteorological aircraft and comparison with particle soot absorption photometer measurements: DOE Southern Great Plains climate research facility and the coastal stratocumulus imposed perturbation experiments, Journal of Geophysical Research: Atmospheres, 111, https://doi.org/10.1029/2005JD005964, _eprint: https://agupubs.onlinelibrary.wiley.com/doi/pdf/10.1029/2005JD005964, 2006.

Bauer, J. J., Yu, X.-Y., Cary, R., Laulainen, N., and Berkowitz, C.: Characterization of the Sunset Semi-Continuous Carbon Aerosol Analyzer, Journal of the Air & Waste Management Association, 59, 826–833, https://doi.org/10.3155/1047-3289.59.7.826, publisher: Taylor & Francis _eprint: https://doi.org/10.3155/1047-3289.59.7.826, 2009.

Baumgardner, D., Raga, G., Peralta, O., Rosas, I., Castro, T., Kuhlbusch, T., John, A., and Petzold, A.: Diagnosing black carbon trends in large urban areas using carbon monoxide measurements, Journal of Geophysical Research: Atmospheres, 107, ICC 4–1–ICC 4–9, https://doi.org/10.1029/2001JD000626, _eprint: https://onlinelibrary.wiley.com/doi/pdf/10.1029/2001JD000626, 2002.

Baumgardner, D., Popovicheva, O., Allan, J., Bernardoni, V., Cao, J., Cavalli, F., Cozic, J., Diapouli, E., Eleftheriadis, K., Genberg, P. J., Gonzalez, C., Gysel, M., John, A., Kirchstetter, T. W., Kuhlbusch, T. a. J., Laborde, M., Lack, D., Müller, T., Niessner, R., Petzold, A., Piazzalunga, A., Putaud, J. P., Schwarz, J., Sheridan, P., Subramanian, R., Swietlicki, E., Valli, G., Vecchi, R., and Viana, M.: Soot reference materials for instrument calibration and intercomparisons: a workshop summary with recommendations, Atmospheric Measurement Techniques, 5, 1869–1887, https://doi.org/https://doi.org/10.5194/amt-5-1869-2012, publisher: Copernicus GmbH, 2012.

Bond, T. and Bergstrom: Light Absorption by Carbonaceous Particles: An Investigative Review, Aerosol Sci. Tecnol., 40, 27–67, https://doi.org/10.1080/02786820500421521, 2006.

Bond, T. C., Anderson, T. L., and Campbell, D.: Calibration and Intercomparison of Filter-Based Measurements of Visible Light Absorption by Aerosols, Aerosol Science and Technology, 30, 582–600, https://doi.org/10.1080/027868299304435, publisher: Taylor & Francis _eprint: https://doi.org/10.1080/027868299304435, 1999.

Bond, T. C., Doherty, S. J., Fahey, D. W., Forster, P. M., Berntsen, T., DeAngelo, B. J., Flanner, M. G., Ghan, S., Kärcher, B., Koch, D., Kinne, S., Kondo, Y., Quinn, P. K., Sarofim, M. C., Schultz, M. G., Schulz, M., Venkataraman, C., Zhang, H., Zhang, S., Bellouin, N., Guttikunda, S. K., Hopke, P. K., Jacobson, M. Z., Kaiser, J. W., Klimont, Z., Lohmann, U., Schwarz, J. P., Shindell, D., Storelvmo, T., Warren, S. G., and Zender, C. S.: Bounding the role of black carbon in the climate system: A scientific assessment, Journal of Geophysical Research: Atmospheres, 118, 5380–5552, https://doi.org/https://doi.org/10.1002/jgrd.50171, _eprint: https://agupubs.onlinelibrary.wiley.com/doi/pdf/10.1002/jgrd.50171, 2013.

525 Brown, S., Minor, H., O'Brien, T., Hameed, Y., Feenstra, B., Kuebler, D., Wetherell, W., Day, R., Tun, R., Landis, E., and Rice, J.: Review of Sunset OC/EC Instrument Measurements During the EPA's Sunset Carbon Evaluation Project, Atmosphere, 10, 287, https://doi.org/10.3390/atmos10050287, 2019.

Bukowiecki, N., Brem, B. T., Wehrle, G., Močnik, G., Affolter, S., Leuenberger, M., Coen, M. C., Hervo, M., Baltensperger, U., and Gysel-Beer, M.: Elucidating local pollution and site representativeness at the Jungfraujoch, Switzerland through parallel aerosol measurements at
530 an adjacent mountain ridge, Environmental Research Communications, 3, 021 001, https://doi.org/10.1088/2515-7620/abe987, publisher: IOP Publishing, 2021.

Burtscher, H.: Physical characterization of particulate emissions from diesel engines: a review, Journal of Aerosol Science, 36, 896–932, https://doi.org/10.1016/j.jaerosci.2004.12.001, 2005.

Cappa, C. D., Zhang, X., Russell, L. M., Collier, S., Lee, A. K. Y., Chen, C.-L., Betha, R., Chen, S., Liu, J., Price, D. J., Sanchez,
535 K. J., McMeeking, G. R., Williams, L. R., Onasch, T. B., Worsnop, D. R., Abbatt, J., and Zhang, Q.: Light Absorption by Ambient Black and Brown Carbon and its Dependence on Black Carbon Coating State for Two California, USA, Cities in Winter and Summer, Journal of Geophysical Research: Atmospheres, 124, 1550–1577, https://doi.org/https://doi.org/10.1029/2018JD029501, _eprint: https://onlinelibrary.wiley.com/doi/pdf/10.1029/2018JD029501, 2019.

Cavalli, F., Viana, M., Yttri, K. E., Genberg, J., and Putaud, J.-P.: Toward a standardised thermal-optical protocol for measuring atmospheric
540 organic and elemental carbon: the EUSAAR protocol, Atmospheric Measurement Techniques, 3, 79–89, https://doi.org/10.5194/amt-3-79-2010, publisher: Copernicus GmbH, 2010.

Chirico, R., DeCarlo, P. F., Heringa, M. F., Tritscher, T., Richter, R., Prévôt, A. S. H., Dommen, J., Weingartner, E., Wehrle, G., Gysel, M., Laborde, M., and Baltensperger, U.: Impact of aftertreatment devices on primary emissions and secondary organic aerosol formation potential from in-use diesel vehicles: results from smog chamber experiments, Atmospheric Chemistry and Physics, 10, 11 545–11 563,
545 https://doi.org/10.5194/acp-10-11545-2010, publisher: Copernicus GmbH, 2010.

Chow, J. C., Watson, J. G., Doraiswamy, P., Chen, L.-W. A., Sodeman, D. A., Lowenthal, D. H., Park, K., Arnott, W. P., and Motallebi, N.: Aerosol light absorption, black carbon, and elemental carbon at the Fresno Supersite, California, Atmospheric Research, 93, 874–887, https://doi.org/10.1016/j.atmosres.2009.04.010, 2009.

Collaud Coen, M., Weingartner, E., Apituley, A., Ceburnis, D., Fierz-Schmidhauser, R., Flentje, H., Henzing, J. S., Jennings, S. G., Moerman,
550 M., Petzold, A., Schmid, O., and Baltensperger, U.: Minimizing light absorption measurement artifacts of the Aethalometer: evaluation of five correction algorithms, Atmospheric Measurement Techniques, 3, 457–474, https://doi.org/10.5194/amt-3-457-2010, publisher: Copernicus GmbH, 2010.

Collaud Coen, M., Andrews, E., Aliaga, D., Andrade, M., Angelov, H., Bukowiecki, N., Ealo, M., Fialho, P., Flentje, H., Hallar, A. G., Hooda, R., Kalapov, I., Krejci, R., Lin, N.-H., Marinoni, A., Ming, J., Nguyen, N. A., Pandolfi, M., Pont, V., Ries, L., Rodríguez, S., Schauer,
555 G., Sellegri, K., Sharma, S., Sun, J., Tunved, P., Velasquez, P., and Ruffieux, D.: Identification of topographic features influencing aerosol observations at high altitude stations, Atmospheric Chemistry and Physics, 18, 12 289–12 313, https://doi.org/10.5194/acp-18-12289-2018, publisher: Copernicus GmbH, 2018.

Corbin, J. C. and Gysel-Beer, M.: Detection of tar brown carbon with a single particle soot photometer (SP2), Atmospheric Chemistry and Physics, 19, 15 673–15 690, https://doi.org/https://doi.org/10.5194/acp-19-15673-2019, publisher: Copernicus GmbH, 2019.

560 Cuesta-Mosquera, A., Močnik, G., Drinovec, L., Müller, T., Pfeifer, S., Minguillón, M. C., Briel, B., Buckley, P., Dudoitis, V., Fernández-García, J., Fernández-Amado, M., Ferreira De Brito, J., Riffault, V., Flentje, H., Heffernan, E., Kalivitis, N., Kalogridis, A.-C., Keernik, H., Marmureanu, L., Luoma, K., Marinoni, A., Pikridas, M., Schauer, G., Serfozo, N., Servomaa, H., Titos, G., Yus-Díez, J., Zioła, N., and

Wiedensohler, A.: Intercomparison and characterization of 23 Aethalometers under laboratory and ambient air conditions: procedures and unit-to-unit variabilities, Atmospheric Measurement Techniques, 14, 3195–3216, https://doi.org/10.5194/amt-14-3195-2021, publisher: Copernicus GmbH, 2021.

Davies, N. W., Cotterell, M. I., Fox, C., Szpek, K., Haywood, J. M., and Langridge, J. M.: On the accuracy of aerosol photoacoustic spectrometer calibrations using absorption by ozone, Atmospheric Measurement Techniques, 11, 2313–2324, https://doi.org/10.5194/amt-11-2313-2018, publisher: Copernicus GmbH, 2018.

Denjean, C., Brito, J., Libois, Q., Mallet, M., Bourrianne, T., Burnet, F., Dupuy, R., Flamant, C., and Knippertz, P.: Unexpected Biomass Burning Aerosol Absorption Enhancement Explained by Black Carbon Mixing State, Geophysical Research Letters, 47, e2020GL089 055, https://doi.org/10.1029/2020GL089055, publisher: John Wiley & Sons, Ltd, 2020.

Di Biagio, C., Formenti, P., Cazaunau, M., Pangui, E., Marchand, N., and Doussin, J.-F.: Aethalometer multiple scattering correction C_{ref} for mineral dust aerosols, Atmospheric Measurement Techniques, 10, 2923–2939, https://doi.org/10.5194/amt-10-2923-2017, publisher: Copernicus GmbH, 2017.

Drinovec, L., Močnik, G., Zotter, P., Prévôt, A. S. H., Ruckstuhl, C., Coz, E., Rupakheti, M., Sciare, J., Müller, T., Wiedensohler, A., and Hansen, A. D. A.: The "dual-spot" Aethalometer: an improved measurement of aerosol black carbon with real-time loading compensation, Atmospheric Measurement Techniques, 8, 1965–1979, https://doi.org/10.5194/amt-8-1965-2015, publisher: Copernicus GmbH, 2015.

Durdina, L., Brem, B. T., Setyan, A., Siegerist, F., Rindlisbacher, T., and Wang, J.: Assessment of Particle Pollution from Jetliners: from Smoke Visibility to Nanoparticle Counting, Environmental Science & Technology, 51, 3534–3541, https://doi.org/10.1021/acs.est.6b05801, publisher: American Chemical Society, 2017.

Durdina, L., Brem, B. T., Schönenberger, D., Siegerist, F., Anet, J. G., and Rindlisbacher, T.: Nonvolatile Particulate Matter Emissions of a Business Jet Measured at Ground Level and Estimated for Cruising Altitudes, Environmental Science & Technology, 53, 12 865–12 872, https://doi.org/10.1021/acs.est.9b02513, publisher: American Chemical Society, 2019.

Forrister, H., Liu, J., Scheuer, E., Dibb, J., Ziemba, L., Thornhill, K. L., Anderson, B., Diskin, G., Perring, A. E., Schwarz, J. P., Campuzano-Jost, P., Day, D. A., Palm, B. B., Jimenez, J. L., Nenes, A., and Weber, R. J.: Evolution of brown carbon in wildfire plumes, Geophysical Research Letters, 42, 4623–4630, https://doi.org/10.1002/2015GL063897, _eprint: https://agupubs.onlinelibrary.wiley.com/doi/pdf/10.1002/2015GL063897, 2015.

Gheusi, F., Durand, P., Verdier, N., Dulac, F., Attié, J.-L., Commun, P., Barret, B., Basdevant, C., Clenet, A., Derrien, S., Doerenbecher, A., El Amraoui, L., Fontaine, A., Hache, E., Jambert, C., Jaumouillé, E., Meyerfeld, Y., Roblou, L., and Tocquer, F.: Adapted ECC ozonesonde for long-duration flights aboard boundary-layer pressurised balloons, Atmospheric Measurement Techniques, 9, 5811–5832, https://doi.org/10.5194/amt-9-5811-2016, publisher: Copernicus GmbH, 2016.

Healy, R. M., Wang, J. M., Jeong, C.-H., Lee, A. K. Y., Willis, M. D., Jaroudi, E., Zimmerman, N., Hilker, N., Murphy, M., Eckhardt, S., Stohl, A., Abbatt, J. P. D., Wenger, J. C., and Evans, G. J.: Light-absorbing properties of ambient black carbon and brown carbon from fossil fuel and biomass burning sources, Journal of Geophysical Research: Atmospheres, 120, 6619–6633, https://doi.org/10.1002/2015JD023382, _eprint: https://onlinelibrary.wiley.com/doi/pdf/10.1002/2015JD023382, 2015.

Healy, R. M., Sofowote, U., Su, Y., Debosz, J., Noble, M., Jeong, C. H., Wang, J. M., Hilker, N., Evans, G. J., Doerksen, G., Jones, K., and Munoz, A.: Ambient measurements and source apportionment of fossil fuel and biomass burning black carbon in Ontario, Atmospheric Environment, 161, 34–47, https://doi.org/10.1016/j.atmosenv.2017.04.034, 2017.

Jacobi, H.-W., Lim, S., Ménégoz, M., Ginot, P., Laj, P., Bonasoni, P., Stocchi, P., Marinoni, A., and Arnaud, Y.: Black carbon in snow in the upper Himalayan Khumbu Valley, Nepal: observations and modeling of the impact on snow albedo, melting, and radiative forcing, The Cryosphere, 9, 1685–1699, https://doi.org/10.5194/tc-9-1685-2015, publisher: Copernicus GmbH, 2015.

Jaffrezo, J.-L., Aymoz, G., Delaval, C., and Cozic, J.: Seasonal variations of the water soluble organic carbon mass fraction of aerosol in two valleys of the French Alps, Atmospheric Chemistry and Physics, 5, 2809–2821, https://doi.org/10.5194/acp-5-2809-2005, publisher: Copernicus GmbH, 2005.

Janssen, N. A., Gerlofs-Nijland, M. E., Lanki, T., Salonen, R. O., Cassee, F., Hoek, G., Fischer, P., Brunekreef, B., and Krzyzanowski, M.: Health effects of black carbon, World Health Organization. Regional Office for Europe, https://apps.who.int/iris/handle/10665/352615, 2012.

Karanasiou, A., Panteliadis, P., Perez, N., Minguillón, M. C., Pandolfi, M., Titos, G., Viana, M., Moreno, T., Querol, X., and Alastuey, A.: Evaluation of the Semi-Continuous OCEC analyzer performance with the EUSAAR2 protocol, Science of The Total Environment, 747, 141 266, https://doi.org/10.1016/j.scitotenv.2020.141266, 2020.

Kirchstetter, T. W., Novakov, T., and Hobbs, P. V.: Evidence that the spectral dependence of light absorption by aerosols is affected by organic carbon, Journal of Geophysical Research: Atmospheres, 109, https://doi.org/10.1029/2004JD004999, _eprint: https://onlinelibrary.wiley.com/doi/pdf/10.1029/2004JD004999, 2004.

Ko, J., Krasowsky, T., and Ban-Weiss, G.: Measurements to determine the mixing state of black carbon emitted from the 2017–2018 California wildfires and urban Los Angeles, Atmospheric Chemistry and Physics, 20, 15 635–15 664, https://doi.org/10.5194/acp-20-15635-2020, publisher: Copernicus GmbH, 2020.

Laborde, M., Mertes, P., Zieger, P., Dommen, J., Baltensperger, U., and Gysel, M.: Sensitivity of the Single Particle Soot Photometer to different black carbon types, Atmospheric Measurement Techniques, 5, 1031–1043, https://doi.org/10.5194/amt-5-1031-2012, publisher: Copernicus GmbH, 2012a.

Laborde, M., Schnaiter, M., Linke, C., Saathoff, H., Naumann, K.-H., Möhler, O., Berlenz, S., Wagner, U., Taylor, J. W., Liu, D., Flynn, M., Allan, J. D., Coe, H., Heimerl, K., Dahlkötter, F., Weinzierl, B., Wollny, A. G., Zanatta, M., Cozic, J., Laj, P., Hitzenberger, R., Schwarz, J. P., and Gysel, M.: Single Particle Soot Photometer intercomparison at the AIDA chamber, Atmospheric Measurement Techniques, 5, 3077–3097, https://doi.org/10.5194/amt-5-3077-2012, 2012b.

Lack, D. A. and Cappa, C. D.: Impact of brown and clear carbon on light absorption enhancement, single scatter albedo and absorption wavelength dependence of black carbon, Atmospheric Chemistry and Physics, 10, 4207–4220, https://doi.org/10.5194/acp-10-4207-2010, publisher: Copernicus GmbH, 2010.

Lack, D. A., Moosmüller, H., McMeeking, G. R., Chakrabarty, R. K., and Baumgardner, D.: Characterizing elemental, equivalent black, and refractory black carbon aerosol particles: a review of techniques, their limitations and uncertainties, Analytical and Bioanalytical Chemistry, 406, 99–122, https://doi.org/10.1007/s00216-013-7402-3, 2014.

Laing, J. R., Jaffe, D. A., and Arthur J. Sedlacek, I. I. I.: Comparison of Filter-based Absorption Measurements of Biomass Burning Aerosol and Background Aerosol at the Mt. Bachelor Observatory, Aerosol and Air Quality Research, 20, 663–678, https://doi.org/10.4209/aaqr.2019.06.0298, publisher: Taiwan Association for Aerosol Research, 2020.

Liousse, C., Cachier, H., and Jennings, S. G.: Optical and thermal measurements of black carbon aerosol content in different environments: Variation of the specific attenuation cross-section, sigma (σ), Atmospheric Environment. Part A. General Topics, 27, 1203–1211, https://doi.org/10.1016/0960-1686(93)90246-U, 1993.

Liu, D., Flynn, M., Gysel, M., Targino, A., Crawford, I., Bower, K., Choularton, T., Jurányi, Z., Steinbacher, M., Hüglin, C., Curtius, J., Kampus, M., Petzold, A., Weingartner, E., Baltensperger, U., and Coe, H.: Single particle characterization of black carbon aerosols at a tropospheric alpine site in Switzerland, Atmospheric Chemistry and Physics, 10, 7389–7407, https://doi.org/10.5194/acp-10-7389-2010, publisher: Copernicus GmbH, 2010.

640   Liu, J., Bergin, M., Guo, H., King, L., Kotra, N., Edgerton, E., and Weber, R. J.: Size-resolved measurements of brown carbon in water and methanol extracts and estimates of their contribution to ambient fine-particle light absorption, Atmospheric Chemistry and Physics, 13, 12 389–12 404, https://doi.org/10.5194/acp-13-12389-2013, publisher: Copernicus GmbH, 2013.

Liu, X., Zheng, M., Liu, Y., Jin, Y., Liu, J., Zhang, B., Yang, X., Wu, Y., Zhang, T., Xiang, Y., Liu, B., and Yan, C.: Intercomparison of equivalent black carbon (eBC) and elemental carbon (EC) concentrations with three-year continuous measurement in Beijing, China,
645   Environmental Research, 209, 112 791, https://doi.org/10.1016/j.envres.2022.112791, 2022.

Lobo, P., Durdina, L., Smallwood, G. J., Rindlisbacher, T., Siegerist, F., Black, E. A., Yu, Z., Mensah, A. A., Hagen, D. E., Miake-Lye, R. C., Thomson, K. A., Brem, B. T., Corbin, J. C., Abegglen, M., Sierau, B., Whitefield, P. D., and Wang, J.: Measurement of Aircraft Engine Non-Volatile PM Emissions: Results of the Aviation-Particle Regulatory Instrumentation Demonstration Experiment (A-PRIDE) 4 Campaign, Aerosol Science and Technology, 49, 472–484, https://doi.org/10.1080/02786826.2015.1047012, publisher: Taylor & Francis
650   _eprint: https://doi.org/10.1080/02786826.2015.1047012, 2015.

Mason, B., Wagner, N. L., Adler, G., Andrews, E., Brock, C. A., Gordon, T. D., Lack, D. A., Perring, A. E., Richardson, M. S., Schwarz, J. P., Shook, M. A., Thornhill, K. L., Ziemba, L. D., and Murphy, D. M.: An intercomparison of aerosol absorption measurements conducted during the SEAC4RS campaign, Aerosol Science and Technology, 52, 1012–1027, https://doi.org/10.1080/02786826.2018.1500012, publisher: Taylor & Francis _eprint: https://doi.org/10.1080/02786826.2018.1500012, 2018.

655   Matsui, H., Hamilton, D. S., and Mahowald, N. M.: Black carbon radiative effects highly sensitive to emitted particle size when resolving mixing-state diversity, Nature Communications, 9, 3446, https://doi.org/10.1038/s41467-018-05635-1, number: 1 Publisher: Nature Publishing Group, 2018.

McMeeking, G. R., Kreidenweis, S. M., Baker, S., Carrico, C. M., Chow, J. C., Collett Jr., J. L., Hao, W. M., Holden, A. S., Kirchstetter, T. W., Malm, W. C., Moosmüller, H., Sullivan, A. P., and Wold, C. E.: Emissions of trace gases and aerosols during the open combus-
660   tion of biomass in the laboratory, Journal of Geophysical Research: Atmospheres, 114, https://doi.org/10.1029/2009JD011836, _eprint: https://agupubs.onlinelibrary.wiley.com/doi/pdf/10.1029/2009JD011836, 2009.

McMeeking, G. R., Fortner, E., Onasch, T. B., Taylor, J. W., Flynn, M., Coe, H., and Kreidenweis, S. M.: Impacts of nonrefractory material on light absorption by aerosols emitted from biomass burning, Journal of Geophysical Research: Atmospheres, 119, 12,272–12,286, https://doi.org/10.1002/2014JD021750, _eprint: https://agupubs.onlinelibrary.wiley.com/doi/pdf/10.1002/2014JD021750, 2014.

665   Metcalf, A. R., Craven, J. S., Ensberg, J. J., Brioude, J., Angevine, W., Sorooshian, A., Duong, H. T., Jonsson, H. H., Flagan, R. C., and Seinfeld, J. H.: Black carbon aerosol over the Los Angeles Basin during CalNex, Journal of Geophysical Research: Atmospheres, 117, https://doi.org/10.1029/2011JD017255, 2012.

Miyakawa, T., Kanaya, Y., Komazaki, Y., Taketani, F., Pan, X., Irwin, M., and Symonds, J.: Intercomparison between a single particle soot photometer and evolved gas analysis in an industrial area in Japan: Implications for the consistency of soot aerosol mass concentration
670   measurements, Atmospheric Environment, 127, 14–21, https://doi.org/10.1016/j.atmosenv.2015.12.018, 2016.

Müller, T., Laborde, M., Kassell, G., and Wiedensohler, A.: Design and performance of a three-wavelength LED-based total scatter and backscatter integrating nephelometer, Atmospheric Measurement Techniques, 4, 1291–1303, https://doi.org/10.5194/amt-4-1291-2011, publisher: Copernicus GmbH, 2011.

Momenimovahed, A. and Olfert, J. S.: Effective Density and Volatility of Particles Emitted from Gasoline Direct In-
jection Vehicles and Implications for Particle Mass Measurement, Aerosol Science and Technology, 49, 1051–1062,
https://doi.org/10.1080/02786826.2015.1094181, publisher: Taylor & Francis _eprint: https://doi.org/10.1080/02786826.2015.1094181,
2015.

Moteki, N. and Kondo, Y.: Dependence of Laser-Induced Incandescence on Physical Properties of Black Carbon Aerosols: Measurements
and Theoretical Interpretation, Aerosol Science and Technology, 44, 663–675, https://doi.org/10.1080/02786826.2010.484450, publisher:
Taylor & Francis _eprint: https://doi.org/10.1080/02786826.2010.484450, 2010.

Nessler, R., Bukowiecki, N., Henning, S., Weingartner, E., Calpini, B., and Baltensperger, U.: Simultaneous dry and ambient mea-
surements of aerosol size distributions at the Jungfraujoch, Tellus Series B Chemical and Physical Meteorology B, 55, 808–819,
https://doi.org/10.1034/j.1600-0889.2003.00067.x, aDS Bibcode: 2003TellB..55..808N, 2003.

Pandolfi, M., Ripoll, A., Querol, X., and Alastuey, A.: Climatology of aerosol optical properties and black carbon mass absorption
cross section at a remote high-altitude site in the western Mediterranean Basin, Atmospheric Chemistry and Physics, 14, 6443–6460,
https://doi.org/10.5194/acp-14-6443-2014, publisher: Copernicus GmbH, 2014.

Peng, J., Hu, M., Guo, S., Du, Z., Zheng, J., Shang, D., Levy Zamora, M., Zeng, L., Shao, M., Wu, Y.-S., Zheng, J., Wang, Y., Glen, C. R.,
Collins, D. R., Molina, M. J., and Zhang, R.: Markedly enhanced absorption and direct radiative forcing of black carbon under pol-
luted urban environments, Proceedings of the National Academy of Sciences, 113, 4266–4271, https://doi.org/10.1073/pnas.1602310113,
publisher: Proceedings of the National Academy of Sciences, 2016.

Petzold, A., Ogren, J. A., Fiebig, M., Laj, P., Li, S.-M., Baltensperger, U., Holzer-Popp, T., Kinne, S., Pappalardo, G., Sugimoto, N., Wehrli,
C., Wiedensohler, A., and Zhang, X.-Y.: Recommendations for reporting "black carbon" measurements, Atmospheric Chemistry and
Physics, 13, 8365–8379, https://doi.org/10.5194/acp-13-8365-2013, publisher: Copernicus GmbH, 2013.

Pileci, R. E., Modini, R. L., Bertò, M., Yuan, J., Corbin, J. C., Marinoni, A., Henzing, B., Moerman, M. M., Putaud, J. P., Spindler, G., Wehner,
B., Müller, T., Tuch, T., Trentini, A., Zanatta, M., Baltensperger, U., and Gysel-Beer, M.: Comparison of co-located refractory black
carbon (rBC) and elemental carbon (EC) mass concentration measurements during field campaigns at several European sites, Atmospheric
Measurement Techniques, 14, 1379–1403, https://doi.org/10.5194/amt-14-1379-2021, 2021.

Raatikainen, T., Brus, D., Hooda, R. K., Hyvärinen, A.-P., Asmi, E., Sharma, V. P., Arola, A., and Lihavainen, H.: Size-selected black
carbon mass distributions and mixing state in polluted and clean environments of northern India, Atmospheric Chemistry and Physics, 17,
371–383, https://doi.org/10.5194/acp-17-371-2017, 2017.

Réveillet, M., Dumont, M., Gascoin, S., Lafaysse, M., Nabat, P., Ribes, A., Nheili, R., Tuzet, F., Ménégoz, M., Morin, S., Picard, G., and
Ginoux, P.: Black carbon and dust alter the response of mountain snow cover under climate change, Nature Communications, 13, 5279,
https://doi.org/10.1038/s41467-022-32501-y, number: 1 Publisher: Nature Publishing Group, 2022.

Samset, B. H., Stjern, C. W., Andrews, E., Kahn, R. A., Myhre, G., Schulz, M., and Schuster, G. L.: Aerosol Absorption: Progress Towards
Global and Regional Constraints, Current Climate Change Reports, 4, 65–83, https://doi.org/10.1007/s40641-018-0091-4, 2018.

Schmid, O., Artaxo, P., Arnott, W. P., Chand, D., Gatti, L. V., Frank, G. P., Hoffer, A., Schnaiter, M., and Andreae, M. O.: Spectral light
absorption by ambient aerosols influenced by biomass burning in the Amazon Basin. I: Comparison and field calibration of absorp-
tion measurement techniques, Atmospheric Chemistry and Physics, 6, 3443–3462, https://doi.org/10.5194/acp-6-3443-2006, publisher:
Copernicus GmbH, 2006.

Schwarz, J. P., Gao, R. S., Fahey, D. W., Thomson, D. S., Watts, L. A., Wilson, J. C., Reeves, J. M., Darbeheshti, M., Baumgard-
ner, D. G., Kok, G. L., Chung, S. H., Schulz, M., Hendricks, J., Lauer, A., Kärcher, B., Slowik, J. G., Rosenlof, K. H., Thomp-

son, T. L., Langford, A. O., Loewenstein, M., and Aikin, K. C.: Single-particle measurements of midlatitude black carbon and light-scattering aerosols from the boundary layer to the lower stratosphere, Journal of Geophysical Research: Atmospheres, 111, https://doi.org/https://doi.org/10.1029/2006JD007076, _eprint: https://onlinelibrary.wiley.com/doi/pdf/10.1029/2006JD007076, 2006.

715 Schwarz, J. P., Spackman, J. R., Fahey, D. W., Gao, R. S., Lohmann, U., Stier, P., Watts, L. A., Thomson, D. S., Lack, D. A., Pfister, L., Mahoney, M. J., Baumgardner, D., Wilson, J. C., and Reeves, J. M.: Coatings and their enhancement of black carbon light absorption in the tropical atmosphere, Journal of Geophysical Research: Atmospheres, 113, https://doi.org/10.1029/2007JD009042, publisher: John Wiley & Sons, Ltd, 2008.

Sciare, J., d'Argouges, O., Sarda-Estève, R., Gaimoz, C., Dolgorouky, C., Bonnaire, N., Favez, O., Bonsang, B., and
720 Gros, V.: Large contribution of water-insoluble secondary organic aerosols in the region of Paris (France) during wintertime, Journal of Geophysical Research: Atmospheres, 116, https://doi.org/10.1029/2011JD015756, _eprint: https://agupubs.onlinelibrary.wiley.com/doi/pdf/10.1029/2011JD015756, 2011.

Sedlacek, A. J. I., Lewis, E. R., Onasch, T. B., Zuidema, P., Redemann, J., Jaffe, D., and Kleinman, L. I.: Using the Black Carbon Particle Mixing State to Characterize the Lifecycle of Biomass Burning Aerosols, Environmental Science & Technology, 56, 14 315–14 325,
725 https://doi.org/10.1021/acs.est.2c03851, publisher: American Chemical Society, 2022.

Segura, S., Estellés, V., Titos, G., Lyamani, H., Utrillas, M. P., Zotter, P., Prévôt, A. S. H., Močnik, G., Alados-Arboledas, L., and Martínez-Lozano, J. A.: Determination and analysis of in situ spectral aerosol optical properties by a multi-instrumental approach, Atmospheric Measurement Techniques, 7, 2373–2387, https://doi.org/10.5194/amt-7-2373-2014, publisher: Copernicus GmbH, 2014.

Sharma, S., Leaitch, W. R., Huang, L., Veber, D., Kolonjari, F., Zhang, W., Hanna, S. J., Bertram, A. K., and Ogren, J. A.: An evaluation of
730 three methods for measuring black carbon in Alert, Canada, Atmospheric Chemistry and Physics, 17, 15 225–15 243, 2017.

Slowik, J. G., Cross, E. S., Han, J.-H., Davidovits, P., Onasch, T. B., Jayne, J. T., Williams, L. R., Canagaratna, M. R., Worsnop, D. R., Chakrabarty, R. K., Moosmüller, H., Arnott, W. P., Schwarz, J. P., Gao, R.-S., Fahey, D. W., Kok, G. L., and Petzold, A.: An Inter-Comparison of Instruments Measuring Black Carbon Content of Soot Particles, Aerosol Science and Technology, 41, 295–314, https://doi.org/10.1080/02786820701197078, publisher: Taylor & Francis _eprint: https://doi.org/10.1080/02786820701197078, 2007.

735 Stein, A. F., Draxler, R. R., Rolph, G. D., Stunder, B. J. B., Cohen, M. D., and Ngan, F.: NOAA's HYSPLIT Atmospheric Transport and Dispersion Modeling System, 96, 2059–2077, https://doi.org/10.1175/BAMS-D-14-00110.1, publisher: American Meteorological Society Section: Bulletin of the American Meteorological Society, 2015.

Subramanian, R., Roden, C. A., Boparai, P., and Bond, T. C.: Yellow Beads and Missing Particles: Trouble Ahead for Filter-Based Absorption Measurements, Aerosol Science and Technology, 41, 630–637, https://doi.org/10.1080/02786820701344589, publisher: Taylor & Francis
740 _eprint: https://doi.org/10.1080/02786820701344589, 2007.

Sun, J., Hermann, M., Yuan, Y., Birmili, W., Collaud Coen, M., Weinhold, K., Madueño, L., Poulain, L., Tuch, T., Ries, L., Sohmer, R., Couret, C., Frank, G., Brem, B. T., Gysel-Beer, M., Ma, N., and Wiedensohler, A.: Long-term trends of black carbon and particle number concentration in the lower free troposphere in Central Europe, Environmental Sciences Europe, 33, 47, https://doi.org/10.1186/s12302-021-00488-w, 2021.

745 Takahama, S., Russell, L. M., Shores, C. A., Marr, L. C., Zheng, J., Levy, M., Zhang, R., Castillo, E., Rodriguez-Ventura, J. G., Quintana, P. J. E., Subramanian, R., Zavala, M., and Molina, L. T.: Diesel vehicle and urban burning contributions to black carbon concentrations and size distributions in Tijuana, Mexico, during the Cal-Mex 2010 campaign, Atmospheric Environment, 88, 341–352, https://doi.org/10.1016/j.atmosenv.2013.09.057, 2014.

Tang, T., Shindell, D., Zhang, Y., Voulgarakis, A., Lamarque, J.-F., Myhre, G., Stjern, C. W., Faluvegi, G., and Samset, B. H.: Response of surface shortwave cloud radiative effect to greenhouse gases and aerosols and its impact on summer maximum temperature, Atmospheric Chemistry and Physics, 20, 8251–8266, https://doi.org/10.5194/acp-20-8251-2020, 2020.

Taylor, J. W., Allan, J. D., Allen, G., Coe, H., Williams, P. I., Flynn, M. J., Le Breton, M., Muller, J. B. A., Percival, C. J., Oram, D., Forster, G., Lee, J. D., Rickard, A. R., Parrington, M., and Palmer, P. I.: Size-dependent wet removal of black carbon in Canadian biomass burning plumes, Atmospheric Chemistry and Physics, 14, 13 755–13 771, https://doi.org/10.5194/acp-14-13755-2014, 2014.

Tinorua, S., Denjean, C., Nabat, P., Bourrianne, T., Pont, V., Gheusi, F., and Leclerc, E.: Two-year measurements of Black Carbon properties at the high-altitude mountain site of Pic du Midi Observatory in the French Pyrenees, EGUsphere, pp. 1–33, https://doi.org/10.5194/egusphere-2023-570, publisher: Copernicus GmbH, 2023.

Tinorua, S., Denjean, C., Nabat, P., Bourrianne, T., Pont, V., Gheusi, F., and Leclerc, E.: Higher absorption enhancement of black carbon in summer shown by 2-year measurements at the high-altitude mountain site of Pic du Midi Observatory in the French Pyrenees, 24, 1801–1824, https://doi.org/10.5194/acp-24-1801-2024, publisher: Copernicus GmbH, 2024.

Wang, R., Balkanski, Y., Boucher, O., Ciais, P., Schuster, G. L., Chevallier, F., Samset, B. H., Liu, J., Piao, S., Valari, M., and Tao, S.: Estimation of global black carbon direct radiative forcing and its uncertainty constrained by observations, Journal of Geophysical Research: Atmospheres, 121, 5948–5971, https://doi.org/10.1002/2015JD024326, _eprint: https://onlinelibrary.wiley.com/doi/pdf/10.1002/2015JD024326, 2016.

Wei, X., Zhu, Y., Hu, J., Liu, C., Ge, X., Guo, S., Liu, D., Liao, H., and Wang, H.: Recent Progress in Impacts of Mixing State on Optical Properties of Black Carbon Aerosol, Current Pollution Reports, 6, 380–398, https://doi.org/10.1007/s40726-020-00158-0, 2020.

Weingartner, E., Saathoff, H., Schnaiter, M., Streit, N., Bitnar, B., and Baltensperger, U.: Absorption of light by soot particles: determination of the absorption coefficient by means of aethalometers, Journal of Aerosol Science, 34, 1445–1463, https://doi.org/https://doi.org/10.1016/S0021-8502(03)00359-8, 2003.

Wong, J. P. S., Tsagkaraki, M., Tsiodra, I., Mihalopoulos, N., Violaki, K., Kanakidou, M., Sciare, J., Nenes, A., and Weber, R. J.: Atmospheric evolution of molecular-weight-separated brown carbon from biomass burning, Atmospheric Chemistry and Physics, 19, 7319–7334, https://doi.org/10.5194/acp-19-7319-2019, publisher: Copernicus GmbH, 2019.

Wu, Y., Yan, P., Tian, P., Tao, J., Li, L., Chen, J., Zhang, Y., Cao, N., Chen, C., and Zhang, R.: Spectral Light Absorption of Ambient Aerosols in Urban Beijing during Summer: An Intercomparison of Measurements from a Range of Instruments, Aerosol and Air Quality Research, 15, 1178–1187, https://doi.org/10.4209/aaqr.2014.09.0224, publisher: Taiwan Association for Aerosol Research, 2015.

Yang, H. and Yu, J. Z.: Uncertainties in Charring Correction in the Analysis of Elemental and Organic Carbon in Atmospheric Particles by Thermal/Optical Methods, Environmental Science & Technology, 36, 5199–5204, https://doi.org/10.1021/es025672z, publisher: American Chemical Society, 2002.

Yu, J. Z., Xu, J., and Yang, H.: Charring Characteristics of Atmospheric Organic Particulate Matter in Thermal Analysis, Environmental Science & Technology, 36, 754–761, https://doi.org/10.1021/es015540q, publisher: American Chemical Society, 2002.

Yus-Díez, J., Bernardoni, V., Močnik, G., Alastuey, A., Ciniglia, D., Ivančič, M., Querol, X., Perez, N., Reche, C., Rigler, M., Vecchi, R., Valentini, S., and Pandolfi, M.: Determination of the multiple-scattering correction factor and its cross-sensitivity to scattering and wavelength dependence for different AE33 Aethalometer filter tapes: a multi-instrumental approach, Atmospheric Measurement Techniques, 14, 6335–6355, https://doi.org/10.5194/amt-14-6335-2021, publisher: Copernicus GmbH, 2021.

Zanatta, M., Gysel, M., Bukowiecki, N., Müller, T., Weingartner, E., Areskoug, H., Fiebig, M., Yttri, K., Mihalopoulos, N., Kouvarakis, G., Beddows, D., Harrison, R., Cavalli, F., Putaud, J., Spindler, G., Wiedensohler, A., Alastuey, A., Pandolfi, M., Sellegri, K., Swietlicki,

E., Jaffrezo, J., Baltensperger, U., and Laj, P.: A European aerosol phenomenology-5: Climatology of black carbon optical properties at 9 regional background sites across Europe, Atmospheric Environment, 145, 346–364, https://doi.org/10.1016/j.atmosenv.2016.09.035, 2016.

790   Zanatta, M., Laj, P., Gysel, M., Baltensperger, U., Vratolis, S., Eleftheriadis, K., Kondo, Y., Dubuisson, P., Winiarek, V., Kazadzis, S., Tunved, P., and Jacobi, H.-W.: Effects of mixing state on optical and radiative properties of black carbon in the European Arctic, Atmospheric Chemistry and Physics, 18, 14 037–14 057, https://doi.org/10.5194/acp-18-14037-2018, 2018.

Zhang, X., Kim, H., Parworth, C. L., Young, D. E., Zhang, Q., Metcalf, A. R., and Cappa, C. D.: Optical Properties of Wintertime Aerosols from Residential Wood Burning in Fresno, CA: Results from DISCOVER-AQ 2013, Environmental Science & Technology, 50, 1681–

795   1690, https://doi.org/10.1021/acs.est.5b04134, publisher: American Chemical Society, 2016.

Zhang, X., Chen, X., and Wang, J.: A number-based inventory of size-resolved black carbon particle emissions by global civil aviation, Nature Communications, 10, 534, https://doi.org/10.1038/s41467-019-08491-9, number: 1 Publisher: Nature Publishing Group, 2019a.

Zhang, Y., Gao, T., Kang, S., and Sillanpää, M.: Importance of atmospheric transport for microplastics deposited in remote areas, Environmental Pollution, 254, 112 953, https://doi.org/10.1016/j.envpol.2019.07.121, 2019b.

800   Zhao, G., Tao, J., Kuang, Y., Shen, C., Yu, Y., and Zhao, C.: Role of black carbon mass size distribution in the direct aerosol radiative forcing, Atmospheric Chemistry and Physics, 19, 13 175–13 188, https://doi.org/10.5194/acp-19-13175-2019, 2019.

Zheng, G., Cheng, Y., He, K., Duan, F., and Ma, Y.: A newly identified calculation discrepancy of the Sunset semi-continuous carbon analyzer, Atmospheric Measurement Techniques, 7, 1969–1977, 2014.